HHS Public Access

Author manuscript

J Comp Neurol. Author manuscript; available in PMC 2022 July 01.

Published in final edited form as:

J Comp Neurol. 2021 July 01; 529(10): 2750–2770. doi:10.1002/cne.25121.

Fractional anisotropy from diffusion tensor imaging correlates with acute astrocyte and myelin swelling in neonatal swine models of excitotoxic and hypoxic-ischemic brain injury

Jennifer K. Lee, MD[1], **Dapeng Liu, PhD**[2], **Dengrong Jiang, PhD**[2], **Ewa Kulikowicz, MS**[1], **Aylin Tekes, MD**[2], **Peiying Liu, PhD**[2], **Qin Qin, PhD**[2], **Raymond C. Koehler, PhD**[1], **Manisha Aggarwal, PhD**[2], **Jiangyang Zhang, PhD**[3], **Lee J. Martin, PhD**[4]

[1]Department of Anesthesiology and Critical Care Medicine, Johns Hopkins University, Baltimore, MD

[2]Department of Radiology, Johns Hopkins University, Baltimore, MD

[3]Department of Radiology, New York University, New York, NY

[4]Department of Pathology, Johns Hopkins University, Baltimore, MD

Abstract

The specific cytopathology that causes abnormal fractional anisotropy (FA) and mean diffusivity (MD) from diffusion tensor imaging (DTI) after neonatal hypoxia-ischemia (HI) is not completely understood. The panoply of cell types in the brain might contribute differentially to changes in DTI metrics. Because glia are the predominant cell type in brain, we hypothesized that changes in FA and MD would signify perturbations in glial microstructure. Using a 3-Tesla clinical scanner, we conducted in vivo DTI MRI in nine neonatal piglets at 20–96 h after excitotoxic brain injury from striatal quinolinic acid injection or global HI. FA and MD from putamen, caudate, and internal capsule in toto were correlated with astrocyte swelling, neuronal excitotoxicity, and white matter injury. Low FA correlated with more swollen astrocytes immunophenotyped by

Corresponding author: Jennifer K. Lee, MD, Johns Hopkins University, Department of Anesthesiology and Critical Care Medicine, 1800 Orleans Street, Room 6321, Baltimore, MD 21287, Office: 410-955-6412, Fax: 410-502-5312, jklee@jhmi.edu.

Author contributions. Jennifer K. Lee: conceptualization; methodology; data acquisition and interpretation; analysis; funding acquisition; writing; approved the manuscript.
Dapeng Liu: conceptualization; methodology; data acquisition and interpretation; writing; approved the manuscript.
Dengrong Jiang: conceptualization; methodology; data acquisition and interpretation; writing; approved the manuscript.
Ewa Kulikowicz: methodology; data acquisition; writing; approved the manuscript.
Aylin Tekes: conceptualization; methodology; data acquisition and interpretation; writing; approved the manuscript.
Peiying Liu: conceptualization; methodology; data acquisition and interpretation; funding acquisition; writing; approved the manuscript.
Qin Qin: conceptualization; methodology; data acquisition and interpretation; writing; approved the manuscript.
Raymond C. Koehler: conceptualization; data interpretation; writing; approved the manuscript.
Manisha Aggarwal: conceptualization; data interpretation; writing; approved the manuscript.
Jiangyang Zhang: conceptualization; data interpretation; writing; approved the manuscript.
Lee J. Martin: conceptualization; methodology; data acquisition; analysis; funding acquisition; writing; approved the manuscript.

Data availability. The data that support the findings of this study are available from the corresponding author upon reasonable request.

Conflict of interest. JKL is a consultant for Edwards Life Sciences.

Ethics approval. All animal protocols were approved by the Johns Hopkins University Animal Care and Use Committee and followed the United States Public Health Service Policy on the Humane Care and Use of Laboratory Animals and the *Guide for the Care and Use of Laboratory Animals*.

aquaporin-4 (AQP4), glial fibrillary acidic protein (GFAP), and glutamate transporter-1 (GLT-1). Low FA was also related to the loss of neurons with perineuronal GLT-1+ astrocyte decorations, large myelin swellings, lower myelin density, and oligodendrocyte cell death identified by 2',3'-cyclic nucleotide 3'-phosphodiesterase, bridging integrator-1, and nuclear morphology. MD correlated with degenerating oligodendrocytes and depletion of normal GFAP+ astrocytes but not with astrocyte or myelin swelling. We conclude that FA is associated with cytotoxic edema in astrocytes and oligodendrocyte processes as well as myelin injury at the cellular level. MD can detect glial cell death and loss, but it may not discern subtle pathology in swollen astrocytes, oligodendrocytes, or myelin. This study provides a cytopathologic basis for interpreting DTI in the neonatal brain after HI.

Graphical Abstract

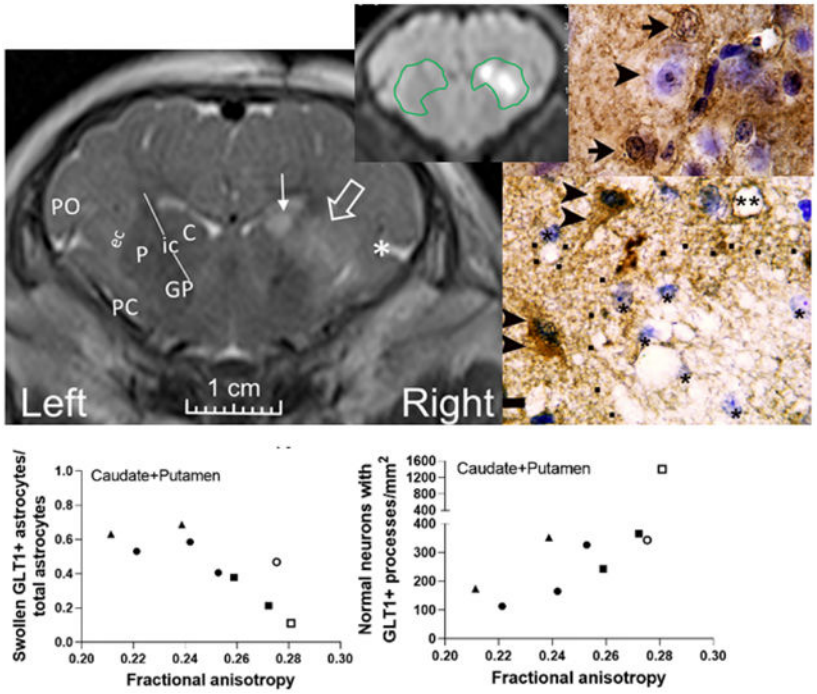

In neonatal piglets with encephalopathy from excitotoxic brain injury, fractional anisotropy from diffusion tensor imaging correlates with swollen astrocytes immunophenotyped by glutamate transporter-1 (GLT-1) and normal neurons with perineuronal GLT-1+ astrocyte decorations in the striatum.

Keywords

newborn; magnetic resonance imaging; oligodendroglia; astrocytes; myelin sheath; aquaporin; GLT-1

1. Introduction

The precise cytopathology that underlies abnormalities in diffusion tensor imaging (DTI) MRI is unclear. Nonetheless, DTI is commonly used to diagnose and predict prognoses in newborn infants with brain injury (Ancora et al., 2013; Carrasco et al., 2018). Hypoxic-ischemic encephalopathy (HIE) from birth asphyxia causes approximately 1 million neonatal deaths worldwide each year (Lawn et al., 2005; Liu et al., 2012). The glutamate receptor-mediated excitotoxicity that occurs from hypoxia-ischemia (HI) (Johnston, 2001) causes varying degrees of regional injury in integral neural cell populations. DTI can provide information about altered tissue architecture and microstructure because it is sensitive to three-dimensional water diffusion. DTI measures the apparent diffusivity of water, which is influenced and hindered by cells and their membranes and organelles. Fractional anisotropy (FA) from DTI measures the anisotropic behavior of water diffusion along multiple directions. Mean diffusivity (MD) measures the average extent of water diffusion over multiple directions. (Farrell et al., 2007; Mori & Zhang, 2006) The cytological interpretation of abnormal FA and MD in HIE (Brissaud et al., 2010; Carrasco et al., 2018) is not definitively understood.

Though cytotoxic edema is known to cause MD to decline (van der Toorn et al., 1996), neuronal and glial injury could have separate contributions. We and others reported that neuronal death correlates with MD after neonatal HI and excitotoxic brain injury (Lee, Liu, et al., 2020; Lodygensky et al., 2011). However, we found that neuronal death had no relationship to FA in injured piglets (Lee, Liu, et al., 2020). Interest is growing in using FA and MD to interrogate gray matter structures, including the development of human cerebral cortex (Maas et al., 2004; Saha et al., 2020). Thus, there is urgency to deciphering DTI's accuracy for detecting gray matter pathology.

Glia comprise at least half of neural cell bodies and a large volume of the non-cell body compartment in the human brain (von Bartheld et al., 2016). They have heterogeneous morphology with up to nine different astrocyte forms, including the well-known protoplasmic, fibrous, and perivascular astrocytes, and at least four different mature oligodendrocyte forms (Rose & Kirchhoff, 2015). Because astroglia do not categorically have isotropic shapes, pathologic glial changes and their influence on the neuropil could heavily affect FA. Moreover, studies with ex vivo high magnetic field MRI indicate that myelination influences DTI (Yano et al., 2018), but little is known about how oligodendrocyte death or myelin injury at the microscopic level affect DTI in the developing brain.

We hypothesized that FA and MD from a 3-Tesla (T) clinical scanner would correlate with perturbations in glial microstructure. We studied piglets that previously showed no relationship between neuronal injury and FA (Lee, Liu, et al., 2020). Here, we focused on glial neuropathology, white matter, and neuronal excitotoxicity in the striatum, which is a subcortical structure with intermingled gray and white matter that is injured in HIE (Carrasco et al., 2018). We interrogated whether DTI correlates with early astrocyte swelling, loss of the astrocyte glutamate transporter 1 (GLT-1) at the astrocyte-neuron

interface, oligodendrocyte degeneration, and myelin injury in neonatal piglets with HI or quinolinic acid (QA)-induced excitotoxic brain injury.

2. Materials and Methods

We investigated piglets from our prior study of neuronal degeneration and MRI (Lee, Liu, et al., 2020) to conserve animals. All protocols were approved by the Animal Care and Use Committee and followed the United States Public Health Service Policy on the Humane Care and Use of Laboratory Animals and the *Guide for the Care and Use of Laboratory Animals*. We published our protocols in detail, including success and failure rates (Lee, Liu, et al., 2020). We provide a methodologic summary here. The data that support the findings of this study are available from the corresponding author upon reasonable request.

2.1. Brain injury

Neonatal male piglets (2–4 days old, 1.0–2.2 kg) received QA-induced brain injury, global HI injury, or sham procedure. They were anesthetized by isoflurane 5% and nitrous oxide 50% in oxygen 50% using a nose cone for intubation and placement of external jugular venous and femoral arterial catheters (Lee, Liu, et al., 2020; Lee, Santos, et al., 2020a). Fentanyl (20 μg/kg bolus+20 μg/kg/h, intravenous [IV]) was administered. Arterial blood pressure, heart rate, rectal temperature, and end-tidal carbon dioxide were continuously monitored. Core temperature was maintained with a warming blanket for a goal of 38.0–39.5°C, which is normothermic for swine (Muns et al., 2013; Panzardi et al., 2013).

Six piglets completed protocols for stereotaxic QA injection–induced excitotoxic brain injury (Lee, Liu, et al., 2020). After intubation, anesthesia was maintained with isoflurane 1–2%, nitrous oxide 70%, and fentanyl. Piglets were positioned in a stereotaxic head frame and secured in a flat skull position with ear bars, mouthpiece, and snout clamp. Bilateral cranial burr holes (2–3 mm in diameter) were drilled 10 mm anterior to the bregma suture and 10 mm lateral to the midline. QA in phosphate-buffered saline (PBS) was injected through a sterile needle secured by a micromanipulator. The QA was slowly delivered 15 mm ventrally to target the putamen, and slow needle penetrations were used to avoid injury above that of the needle track. Piglets received 240 nmol (4 μL), 720 nmol (12 μL), or 960 nmol (16 μL) injections of QA into the right putamen. PBS in equal volume was injected into the left putamen as a control. Piglets emerged from anesthesia and recovered for 20 to 96 h until their MRI.

Three additional piglets were randomized to the global HI or sham procedure protocols (Lee, Santos, et al., 2020b; Lee et al., 2016; Santos et al., 2018; Wang et al., 2015; Wang et al., 2016). For these piglets, the isoflurane was discontinued after the venous and arterial catheters were placed. The anesthetic consisted of nitrous oxide 70% in oxygen 30% and fentanyl. Vecuronium 0.2 mg/kg (IV) was administered to prevent ventilatory effort during hypoxia-asphyxia. Hypoxia was induced by lowering the inhaled oxygen concentration to 10% for 45 min. Five minutes of room air was then provided to briefly reoxygenate the heart, a necessary step for cardiac resuscitation. Then, the endotracheal tube was clamped for 8 min to induce asphyxia. The piglets were resuscitated by chest compressions, oxygen 50%, and epinephrine 100 μg/kg IV. Piglets that did not resuscitate within 3 min were

excluded. The sham protocol included the same anesthetic and provision of oxygen 50% for 3 min (to match the oxygen 50% given during chest compressions in HI piglets). The oxygen was then reduced to 30% in nitrous oxide 70% after resuscitation or time equivalent in shams. Anesthesia was continued for 3 more hours to allow the neuromuscular blockade to wear off and for piglets to regain hemodynamic stability. The piglets were extubated and recovered for 22 to 45 h until their MRI.

To re-induce anesthesia for MRI, piglets received isoflurane and nitrous oxide/oxygen for tracheostomy to bypass potential post-extubation laryngeal edema from the first intubation. They were then transitioned to a total IV anesthetic of fentanyl (100 μg/kg/h, plus as-needed 12.5 mcg/kg boluses and infusion increases by 12.5 mcg/kg/h) and propofol (7.5 mg/kg/h plus as-needed 1–2 mg/kg boluses and infusion increases by 2 mg/kg/h). Dopamine was provided beginning at 5 μg/kg/min as needed to maintain the mean arterial blood pressure ≥45 mmHg and minimize the risk of cerebral hypoperfusion (Larson et al., 2013). This second anesthetic for MRI does not cause brain injury (Lee, Liu, et al., 2020). Mechanical ventilation with oxygen/air 50%/50% maintained normocapnia, arterial blood pressure and heart rate were continuously monitored, and vital signs were recorded every 15 min during the MRI scan.

2.2. In vivo MRI

DTI was obtained on a 3T clinical scanner (Prisma; Siemens, Erlangen, Germany) and 15-channel knee coil. We previously reported our sequence parameters (Lee, Liu, et al., 2020), which are derived from the Human Connectome Project protocol (90 diffusion encoding directions and b values of 1000, 2000, and 3000 s/mm^2) (Van Essen et al., 2013). We used 95 non-collinear diffusion encoding directions and three b-shells with effective b-values of 650, 1350, and 2000 s/mm^2 to accommodate the higher tissue diffusivity of immature brains relative to that of adults (Neil et al., 1998). Single-shot, diffusion-weighted, spin-echo echo-planar imaging sequences were obtained with TR=4800 ms; TE=73 ms; in-plane matrix size=128×128; and NEX=2 (imaging time 16 min). Three piglets had imaging with 1×1 mm^2 in-plane resolution (40 slices of 1.5 mm thickness and FOV=128×128 mm^2), and six piglets were imaged with 1.2×1.2 mm^2 in-plane resolution (50 slices of 1.2 mm thickness and FOV=154×154 mm^2) with GRAPPA factor=2. We made this change to generate isotropic voxel size. FA and MD should not be substantially affected by the 15% voxel volume increase and signal-to-noise ratio (Farrell et al., 2007). The piglets remained anesthetized to prevent movement. MD and FA maps were calculated by vendor-specific software.

We anatomically matched coronal images to anterior striatal neuropathology slides to evaluate DTI and neuropathology in counterpart regions of interest (ROI). Investigators who were blinded to the neuropathology and treatment manually drew a single ROI around putamen, caudate, and internal capsule to measure FA and MD (Figure 1) (Lee, Liu, et al., 2020). The piglet internal capsule consists of discontinuous white matter fascicles with penetrating isthmi of putamen and caudate gray matter between the fascicles (Figure 2) (Martin, Brambrink, Koehler, et al., 1997). This structural overlap of gray and white matter within the internal capsule region is distinct from that of human and non-human primates

(Martin et al., 1991). Because 3T MRI cannot clearly distinguish the piglet's internal capsule fascicles from interjacent gray matter, we analyzed a single ROI encompassing putamen, caudate, and internal capsule (Lee, Liu, et al., 2020). A neuropathologist with 36 years of neuropathology and 20 years of MRI experience (LJM) and an MRI physicist with 10 years of MRI experience (DL) measured FA on the DTI map co-registered to the T2-weighted image using OsiriX DICOM Viewer software in consensus. A pediatric neuroradiologist (AT) with 12 years of neonatal brain MRI experience and 19 years of clinical and research MRI experience and a neuropathologist (LJM) measured MD using the Picture Archiving and Communication System in consensus. Only the right brain was analyzed.

2.3. Neuropathology

Immediately after the MRI, piglets were euthanized with pentobarbital 50 mg/kg and phenytoin 6.4 mg/kg IV and transcardially-intraaortically perfused with cold PBS followed by 4% paraformaldehyde. The heads were immersed in 4% paraformaldehyde for 12–24 h for further in situ brain fixation. Then, the brains were removed from the skull and immersion post-fixed in 4% paraformaldehyde for 1–2 weeks. The brains were blocked in the coronal plane using precise anatomical landmarks to make consistent slabs, paraffin embedded, and cut into 10-μm-thick coronal sections for immunohistochemistry (IHC).

2.4. IHC

We used an IHC protocol that we have reported in detail (Lee, Santos, et al., 2020b; Lee et al., 2016; Santos et al., 2018). After deparaffinization and antigen retrieval with 10 mM sodium citric acid and 0.05% Tween 20 at pH 6.0, the slides were blocked with 3% normal goat serum. The primary antibodies are listed in Table 1. We immunophenotyped astrocytes using primary antibodies for aquaporin 4 (AQP4,1:25, anti-rabbit, LS Bio, Seattle, WA, catalog number LS-B11637), glial fibrillary acidic protein (GFAP; 1:200, anti-rabbit, Agilent Dako, Santa Clara, CA, catalog number Z 0334, Research Resource Identifier (RRID): AB_10013382), and GLT-1 (1:100, anti-rabbit, developed and validated by LJM and used in multiple publications) (Furuta et al., 1997; Ginsberg et al., 1996; Martin, Brambrink, Lehmann, et al., 1997; Northington et al., 1999; Northington et al., 1998). Oligodendrocytes were identified by primary antibodies for bridging integrator-1 (BIN1; 1:200, anti-rabbit, Proteintech, Rosemont, IL, catalog number 14647-1-AP, RRID: AB_2243396) as a marker of mature, myelinating oligodendrocytes (De Rossi et al., 2016; Lee, Santos, et al., 2020b) and 2′,3′-cyclic nucleotide 3′-phosphodiesterase (CNPase) as a marker of oligodendrocytes and their myelinating processes (1:50, anti-mouse, Millipore Sigma, Burlington, MA, catalog number MAB326, RRID:AB_2082608) (Verrier et al., 2013). Non-immune IgG of the same isotype and concentration was substituted for the primary antibody to generate negative controls. The slides were incubated with goat anti-rabbit IgG (1:20, Sigma Aldrich, St. Louis, MO) secondary antibody and rabbit peroxidase anti-peroxidase soluble complex antibody (1:100, Sigma-Aldrich) or goat anti-mouse (1:20, Sigma Aldrich) and mouse peroxidase anti-peroxidase soluble complex antibody (1:100, Sigma-Aldrich). Immunoreactive cells and myelin sheaths were identified as dark brown after the slides were developed with hydrogen peroxide as the substrate and 3,3′-

diaminobenzidine as the chromogen. We also lightly counterstained the slides with cresyl violet to identify nuclear and other cellular features as blue.

2.5. Antibody characterization

Full-length western blots confirmed that the BIN1 and CNPase antibodies identify a mono-specific immunoreactive band at the expected molecular weight in piglet brain (data not shown). We also published that the BIN1 antibody has strong immunoreactivity for piglet oligodendrocytes by IHC (Lee, Santos, et al., 2020a). The GFAP antibody is mono-specific on western blot (Lesuisse & Martin, 2002). The GLT-1 antibody was developed, characterized, and validated by LJM and used in multiple peer reviewed neuropathology manuscripts (Furuta et al., 1997; Ginsberg et al., 1996; Martin, Brambrink, Lehmann, et al., 1997; Northington et al., 1999; Northington et al., 1998). The AQP4 antibody was commercially validated using an immunogenic blocking peptide by the vendor.

2.6. Microscopic cytopathology

An investigator (JKL) with 10 years of experimental neuropathology experience counted swollen cells and myelin processes in slides anatomically matched to the DTI image at an anterior striatal level (Figure 1). An experimental neuropathologist with decades of experience screened the slides for counterreliability (LJM). Both were blinded to the MRI images, DTI, and treatment. We analyzed one slide per pig for each antibody. We used cell profile counting rather than stereology to maximize the use of multiple glial antibodies for diagnostic neuropathology and to prepare separate brain tissue samples for an arterial spin labeling cerebral perfusion study that is not reported here.

Astrocytes with AQP4+ aggregates (large clusters of AQP4 immunoreactivity) were counted in 12 microscope fields in putamen and 12 fields in caudate at 1000x with oil immersion. The microscope fields were placed in a Z-pattern to capture the full dorsal-ventral and central aspects of putamen and caudate. Astrocytes without AQP4+ aggregates were classified as AQP4-negative and identified by their nuclear morphology. We additionally classified the astrocytes as swollen or not swollen. Because AQP4 expression varies by injury severity and has a complex relationship to blood-brain barrier integrity (Rodriguez-Grande et al., 2018), we classified astrocytes as not swollen rather than using the term normal.

GFAP+ astrocytes were counted in 10 fields each for putamen and caudate at 400x in a Z-pattern. Slides stained for GLT-1 were counted at 1000x with oil immersion in 12 fields each spanning the putamen and caudate. Normal and swollen GLT-1+ astrocytes, neurons with peri-neuronal GLT-1+ decorations, and GLT-1+ neurons were counted. Piglet striatal neurons are normally not positive for GLT-1, but HI causes them to express GLT-1 with excitotoxic death (Martin, Brambrink, Lehmann, et al., 1997). We also estimated astrocyte cell body swelling using volume=$\pi/6$ (ab^2) where a is the cell body's major axis diameter and b is the minor axis diameter (Martin et al., 1986).

Oligodendrocytes and their myelinating processes were analyzed by CNPase and BIN1 IHC. Ten fields spanning putamen and 10 fields spanning caudate were counted at 400x. In putamen, every microscope field included at least part of a white matter bundle, and CNPase

+ and BIN1+ cells were counted in both white and gray matter. Because caudate has fewer white matter bundles, cell counts were largely conducted in gray matter parenchyma. Recently replicated doublet cells counted as two cells. Additionally, we measured the first three bundles of the internal capsule along the dorsal aspect of the lateral ventricle at the corpus callosum-striatum junction using ImageJ (Fiji, v. 1.52p, National Institutes of Health, Bethesda, MD). Cell counts were obtained throughout the entire three white matter bundles and then divided by the bundles' sum area.

We also counted CNPase+ myelin processes with central pallor from swelling and that exceeded 6.25 μm in greatest diameter at 1000x with oil immersion. The number of myelin swellings throughout the first three internal capsule bundles was divided by the bundles' sum area. Myelin swellings in the gray matter parenchyma were also counted in 10 microscope fields each in putamen and caudate. Myelin swellings were not counted in white matter bundles within the putamen or caudate.

2.7. Myelin Luxol fast blue (LFB) staining

LFB identifies greater myelin density as darker azure (Lee, Santos, et al., 2020b; Warntjes et al., 2017). All slides were placed into the same rack to ensure equal staining and rinsing. Paraffin-embedded sections that were anatomically matched to the DTI images were uniformly cut into 10-μm-thick sections, deparaffinized, and incubated in LFB (0.1 g in 100 mL 95% ethanol) as we previously reported (Lee, Santos, et al., 2020b). After being rinsed in 95% ethanol and distilled water, the sections were developed by lithium carbonate (0.05 g in 100 mL distilled water) and 70% ethanol followed by a light cresyl violet counterstain. The slides were scanned without magnification in identical lighting (Hewlett-Packard Scanjet 5590; Palo Alto, CA). One investigator (JKL) who was blinded to the MRI images, DTI, and treatment, used ImageJ to outline an ROI encompassing the putamen, caudate, and internal capsule (Figure 2). The inverse, integrated density measurement was analyzed so that a higher value corresponded with darker azure staining and greater myelin density.

2.8. Statistics

We compared the number of AQP4+ astrocytes (swollen or non-swollen) and the number of GLT-1+ astrocytes (normal or swollen) to FA and MD. We also analyzed the astrocyte counts as ratios to total number of astrocytes, which was the sum of all AQP4- (or GLT-1−) negative and positive astrocytes. For astrocytes immunophenotyped by GFAP, we evaluated the number of normal, swollen, and degenerating GFAP+ astrocytes in addition to their ratios to total GFAP+ astrocytes. The number of normal neurons with GLT-1+ processes on the cytoplasmic membrane; the number of degenerating, GLT-1+ neurons; and the ratios of normal- and degenerating-to-total GLT-1+ neurons were analyzed. We also compared normal, apoptotic, degenerating, and doublet CNPase+ or BIN1+ cell counts and their ratios to total CNPase+ or BIN1+ cells to the DTI scalars.

Graphs were generated and data were analyzed in GraphPad (v.8, San Diego, CA). We compared cell counts and ratios to FA and MD using Spearman correlations. Significance was assumed for $p<0.05$. This is a secondary analysis of a cohort that was designed with a sample size powered to correlate neuronal death with MD (Lee, Liu, et al., 2020).

3. Results

One piglet received 240 nmol QA with 96-h recovery; three received 720 nmol with 20-, 91-, and 96-h recoveries; and two received 960 nmol with 24- and 25-h recoveries before their MRI. Two piglets received HI injury with 45-h recoveries and one received sham procedure with 23-h recovery until their MRI. We previously reported the piglets' physiology (Lee, Liu, et al., 2020). Briefly, the hypoxia-asphyxia protocol to induce global HI caused oxyhemoglobin saturations of 4.3% and 4.9%, pH 6.84 and 6.90, and $PaCO_2$ 115 and 110 mmHg. The pigs recovered to normoxia and normocapnia prior to extubation. During the MRI, piglets had mean arterial blood pressures of 66 mmHg (standard deviation [SD], 15), heart rate 102 beats per minute (SD, 31), and end-tidal CO_2, 44 mmHg (SD, 11).

3.1. DTI correlates with astrocyte and neuron cytopathology

AQP4+ swollen astrocytes had cytoplasmic expansion that rendered the cytoplasm clear or pale with or without cytoplasmic content reticulations, vacuoles, and enlarged cell soma delineated by AQP4 aggregates (Figure 3a, b). Non-swollen AQP4+ astrocytes were generally 198.6–426.2 μm^3. Swollen AQP4+ astrocytes were approximately 1248.0–1647.4 μm^3.

Normal GFAP+ astrocytes had normal-appearing nuclear chromatin, a centrally positioned nucleus, intact processes, and normal-appearing cytoplasm (Figure 3c). Swollen GFAP+ astrocytes had cytoplasmic swelling; residual reticulated GFAP immunoreactivity in the cytoplasm or GFAP immunoreactivity that was marginalized to the cytoplasmic periphery; vacuoles; and either nuclear swelling or an attritional nucleus that was eccentrically positioned consistent with our published criteria (Martin, Brambrink, Lehmann, et al., 1997) (Figure 3d, f). Non-swollen GFAP+ astrocytes were approximately 145.3–150.0 μm^3. Swollen GFAP+ astrocytes were 2199.7–3369.6 μm^3. Degenerating GFAP+ astrocytes had a condensed cell body, pyknotic nucleus, dense GFAP nuclear staining, and often clasmatodendrosis (astrocyte process fragmentation) (Figure 3e, f).

Astrocyte morphology from AQP4 immunostaining was associated with FA. The number of non-swollen, AQP4+ astrocytes (r=0.800; p=0.014) and their ratio to total astrocyte numbers (r=0.933, p=0.001) in putamen correlated with FA in the ROI encompassing the putamen, caudate, and internal capsule (Figure 4a, b). Non-swollen AQP4+ astrocytes (r=0.820, p=0.010) and the ratio to total astrocytes (r=0.850, p=0.006) in caudate also correlated with FA (Figure 4c, d). Similar relationships were identified when astrocyte counts were summed from putamen and caudate (non-swollen AQP4+ astrocytes: r=0.867, p=0.005; ratio: r=0.900, p=0.002; Figure 4e, f). FA was also related to swollen astrocytes. More swollen AQP4+ astrocytes in putamen (r= −0.800, p=0.014) and a higher sum ratio of swollen to total astrocytes in putamen and caudate (r= −0.800, p=0.014) correlated with lower FA (Figure 4g, h). In contrast, the same astrocyte metrics had no relationship to MD (Figure 5a–h).

MD was related to the number of normal GFAP+ astrocytes in putamen (r=0.700; p=0.043) and in caudate and putamen combined (r=0.717; p=0.037; Figure 4i, j), whereas FA was not (Figure 5i, j). GFAP immunostaining corroborated the AQP4+ astrocyte data. The number of

swollen GFAP+ astrocytes (r= −0.900; p=0.002) and its ratio to total GFAP+ astrocytes (r= −0.933; p<0.001) in putamen correlated with FA (Figure 4k, l). However, these data showed no relationship to MD (Figure 5k, l). Degenerating GFAP+ astrocytes were not associated with either DTI scalar.

GLT-1+ astrocytes had brown granules in their cytoplasm and nucleus and plasma membrane immunoreactivity. Normal astrocytes, whether GLT-1+ or GLT-1− negative, had normal cell size (Figure 6a, c). Swollen GLT-1+ or GLT-1-negative astrocytes had cytoplasmic swelling with vacuoles (Figure 6b, d). GLT-1+ astrocyte swelling was on a similar size scale as the swollen GFAP+ astrocytes.

FA correlated with the number of normal GLT-1+ astrocytes (r=0.750; p=0.026) and the ratio of normal GLT-1+ astrocytes to total astrocytes (r=0.800; p=0.014) in putamen. When the cell counts from putamen and caudate were summed, the normal GLT-1+ astrocytes (r=0.833; p=0.008) and ratio (r=0.817; p=0.011) were also related to FA. As with AQP4 and GFAP, the ratios of swollen GLT-1+ astrocytes to total astrocytes in putamen (r= −0.800; p=0.014) and caudate plus putamen (r= −0.817; p=0.011) correlated with FA (Figure 7a–f). The same GLT-1 astrocyte cytology measures were unrelated to MD (Figure 8a–f).

Normal neurons with GLT-1 processes contacting their cytoplasmic membrane had a large nucleus (~8–10 μm in diameter), at least one small nucleolus or nuclear gems (Cajal bodies), normal chromatin, normal-appearing cytoplasm, and large round cell body (Figure 6a, c). Degenerating GLT-1+ striatal neurons had nuclear pyknosis and GLT-1 enrichment in the cytoplasm (Figure 6b, d).

The number of normal neurons with GLT-1+ processes on their plasma membrane in putamen (r=0.900; p=0.002) and in caudate combined with putamen (r=0.717; p=0.037) correlated to FA. The ratio of normal neurons with GLT-1+ processes along the cell membrane to the total neuron count in putamen was also associated with FA (r= 0.800; p=0.014; Figure 7g–i). These relationships were not observed with MD (Figure 8g–i). There was no association between degenerating GLT-1+ neurons and either DTI scalar.

3.2. DTI correlates with oligodendrocyte and myelin pathology

Normal CNPase+ oligodendrocytes (Figure 9a) had a normal-appearing, open nucleus and often brown processes extending from the cell body (Figure 9b). Apoptotic CNPase+ cells had karyorrhectic nuclear fragmentation with condensation into round apoptotic bodies consistent with previous electron microscopic demonstrations (Martin et al., 1998) (Figure 9e). In putamen and caudate, recently divided doublet cells had normal and adjacent nuclei, overlapping cytoplasm from closely apposed pairs of cells, and slightly invaginated cell membranes reminiscent of final telophase (Figure 9d). CNPase+ processes with myelin swellings and central pallor are shown in Figures 9c, e, and f.

Normal BIN1+ oligodendrocytes had a normal-appearing nucleus, brown staining in the nucleus and cytoplasm, and often brown processes extending from the cell body (Figure 10a, d, e). Degenerating BIN1+ oligodendrocytes had vacuoles in the nucleus, cell soma, and/or

processes (Figure 10b, c). Apoptotic BIN1+ cells had karyorrhectic nuclear fragmentation (Figure 10f).

In the internal capsule, the number of large, CNPase+ myelin swellings correlated with FA (r= −0.833; p=0.008; Figure 11a) but not MD (Figure 12a). However, MD and degenerating BIN1+ cells were related (cell count: r= −0.696, p=0.046; ratio to total BIN1+ cells: r= −0.696, p=0.046; Figure 11b, c). By contrast, FA was not associated with BIN1+ cellular degeneration (Figure 12b, c). In the caudate, the ratios of normal-to-total CNPase+ cells (r=0.695; p=0.045), doublet-to-total CNPase+ cells (r=0.695, p=0.045), apoptotic-to-total CNPase+ cells (r= −0.695, p=0.045), and apoptotic-to-total BIN1+ cells (r= −0.763, p=0.024) correlated with FA but not MD (Figure 11d–g, Figure 12d–g). Finally, myelin density assessed by LFB stain in the internal capsule, caudate, and putamen was related to FA (r=0.733, p=0.031; Figure 11h).

4. Discussion

DTI is increasingly used to diagnose and predict outcomes of neonatal HIE (Ancora et al., 2013; Carrasco et al., 2018). Although DTI delineates regional brain damage, there is scant information on the relationships between FA, MD, and glial injury at the cellular level of resolution. Because the glia-to-neuron ratio increases with forebrain size (Herculano-Houzel, 2014), glia could significantly affect DTI in gyrencephalic brain. We tested whether in vivo DTI using a 3T clinical scanner is associated with glial microstructure and myelin at the microscopic level in a clinically relevant, large animal model of neonatal HIE. We previously showed that MD, but not FA, is associated with neuronal degeneration after excitotoxic and HI brain injury in piglets (Lee, Liu, et al., 2020). Here, we found that FA correlated with more swollen astrocytes in caudate and putamen. MD was not sensitive to astrocyte swelling but it was associated with the loss of GFAP+ astrocytes. FA was also related to large myelin swellings in the internal capsule, myelin loss in the internal capsule and striatum, and oligodendrocyte apoptosis in the caudate. By contrast, MD was only associated with degenerating myelinating oligodendrocytes in the internal capsule. Thus, astrocyte cytotoxic edema and swelling, myelin swelling, and oligodendrocyte apoptosis are significantly related to FA in the newborn brain. MD only correlated with fulminant glial degeneration and loss.

Piglets recovered for 20 to 96 h after QA injection, HI injury, or sham procedure until their MRI, which was followed by immediate brain perfusion-fixation for neuropathology. We focused on the subacute recovery period to study early injury evolution. Additionally, the postnatal window for therapeutic hypothermia is the first 4 days after birth for HIE. Obtaining brain MRIs during therapeutic hypothermia is being clinically investigated as an early prognostic biomarker for brain injury severity. (Lucke et al., 2019; Shetty et al., 2019) Piglets were studied at different time points to examine how the cytopathology in different striatal cell types relate to changes in clinical DTI. Though the excitotoxic QA and HI injuries are both acute in onset, the subsequent evolution of cellular injury is not synchronous. The damaged cells are not uniformly at the same stage of injury. Time constancy creates limitations when investigating asynchronous cellular injury and

degeneration in vivo. Thus, we used multiple time points to better interrogate the neuropathology of our experimental model.

We used piglet models of excitotoxic brain injury from stereotaxic QA injection (Lee, Liu, et al., 2020) and global HI (Lee et al., 2016; Martin & Wong, 2013; Santos et al., 2018; Wang et al., 2015; Wang et al., 2016). Brain development at term gestation, perinatal growth, connectivity, and prenatal and extended postnatal myelination are analogous in humans and piglets (Borsani et al., 2019; Bozek et al., 2018; de Graaf-Peters & Hadders-Algra, 2006; Dobbing & Sands, 1979; Ishibashi et al., 2012; Lee, Santos, et al., 2020a; Mudd & Dilger, 2017; Oishi et al., 2012; Sheng et al., 1989; Simchick et al., 2019; Siu et al., 2015; Sweasey et al., 1976). We created the piglet model of QA-induced excitotoxicity (Lee, Liu, et al., 2020; Portera-Cailliau et al., 1997) because excitotoxicity is a key mechanism of HI brain injury (Johnston, 2005). QA is also involved in several human neurologic diseases, including autism, Alzheimer's disease, Huntington's disease, depression, and amyotrophic lateral sclerosis (Lugo-Huitrón et al., 2013). We focused on putamen, caudate, and internal capsule because these regions are commonly injured in human and piglet HIE (Carrasco et al., 2018; Koehler et al., 2018; Lee et al., 2017; Martin, Brambrink, Koehler, et al., 1997; Tekes et al., 2015)

4.1. Astrocytes

Astrocytes rapidly change their cell volume after injury, and they have high surface-to-volume ratios (Hama et al., 2004). They regulate water, ionic, and glutamate homeostasis. We used three antibodies to distinguish the astrocyte water channels, neurotransmitter transporters, and cytoskeletal proteins. AQP4 immunophenotyped astrocytes that regulate water, GLT-1 identified astrocytes active in excitatory neurotransmission and glutamate re-uptake, and GFAP was a corroborating marker for astrocytes and their processes in the perivascular and parenchymal compartments. More swollen AQP4+, GLT-1+, and GFAP+ astrocytes in putamen and caudate correlated with lower FA. The significant influence of disrupted glial parenchymal microstructure on FA agrees with the fact that astroglial processes predominantly organize the brain's matrix (von Bartheld et al., 2016). However, we cannot conclude whether AQP4, GLT-1, or GFAP astrocyte changes directly contribute to DTI or whether they are bystander effects of other cellular and molecular pathology that drive changes in DTI. In the future, we can clarify these issues using conditional virus-mediated genetic manipulations in piglets (Santos et al., 2018) to target specific proteins and cells to modulate DTI changes during evolving encephalopathy.

AQP4 is the most abundant aquaporin in mammalian brain. It facilitates cellular transmembrane water transport and is located predominantly in astrocytes that maintain brain-blood interfaces and regulate the flow of interstitial fluid (Potokar et al., 2016). AQP4 accumulates in astrocyte endfeet that interface with vessels (Rosito et al., 2018), and it relocalizes to the astrocyte processes after brain trauma (Rodriguez-Grande et al., 2018). We also observed AQP4 redistribution to the processes of swollen astrocytes, often in close proximity to vacuoles (Figure 3b). In injured astrocytes, AQP4 appeared mislocalized and aggregated. These AQP4 aggregations are associated with loss of function, disease, and cell death (Jablonski et al., 2004; Rosito et al., 2018). Though the AQP4+ labeling in astrocyte

endfeet appeared perivascular and suggested minimal vasogenic edema in the same microscope fields with swollen astrocytes (Figure 3f), electron microscopy is needed to confirm tight endfeet-to-vessel associations and endothelial integrity. Vasogenic edema that we did not observe could have contributed to high T2 in some piglets (Figure 1a). Nonetheless, our data identify an important relationship between cytotoxic edema from AQP4+ astrocyte swelling and FA. The wholesale tissue edema is apparent in the lateral ventricle's loss of patency in the dorsolateral region from the caudate nucleus' expansion (Figure 1a).

MD was not associated with swelling in AQP4+ astrocytes. Another study linked shifted apparent diffusivity and AQP4 inhibition in adult mice with a 11.7T scanner (Debacker et al., 2020). MD has also been interrogated with AQP1 overexpression in an artificial cell system using a 7T scanner (Mukherjee et al., 2016). Cortical gray matter damage based on glial reactivity correlated with MD in neonatal rats with hydrocephalus using a 7T scanner (Yuan et al., 2010). It is difficult to compare our piglet work using a 3T clinical scanner to these studies. Astrocyte morphology and the extent that astrocyte processes organize the neuropil vary by species. For example, human protoplasmic astrocytes have a 2.6-fold greater diameter and 10-fold increase in astrocyte processes compared to rodent astrocytes (Oberheim et al., 2009). The increase in glia-to-neuron ratio that occurs during brain development (von Bartheld et al., 2016) also influences how astrocytes affect DTI.

Though GFAP colocalizes with AQP4 (Tomás-Camardiel et al., 2004), it identified different morphologic astrocyte features. Some GFAP+ astrocytes are protoplasmic and parenchymal without perivascular functions, and they do not regulate blood-brain barrier permeability (Rodriguez-Grande et al., 2018). As with AQP4, only FA correlated with swollen GFAP+ astrocytes in putamen. MD was associated with the number of normal GFAP+ astrocytes but not swollen astrocytes in caudate and putamen. We previously found that MD distinguishes normal neurons from those undergoing end-stage cell death but does not measure sublethally injured neurons with cytoplasmic vacuoles (Lee, Liu, et al., 2020). Here, we confirmed that MD is related to fulminant astrocyte loss whereas MD does not seem to detect astrocyte changes that may be nonlethal. Clasmatodendrosis from astrocyte process fragmentation (Figure 3e, f) likely affected the DTI scalars, though we did not quantify the clasmatodendrosis.

GLT-1 immunostaining served two purposes: to identify astrocytes involved in glutamate reuptake and to provide mechanistic insight into excitotoxic brain injury. GLT-1 identified astrocytes involved in extracellular glutamate reuptake. Astrocyte glutamate transporters dissipate excitatory neurotransmission to protect neurons from excessive synaptic glutamate exposure (Bylicky et al., 2018). Loss of GLT-1 function causes abnormal brain network activity on diffusion functional MRI (Abe et al., 2020).

Higher FA correlated with more normal GLT-1+ astrocytes in putamen and caudate, and lower FA was associated with more swollen GLT-1+ astrocytes. The identified relationship between the GLT-1+ astrocyte population and FA concurs with the prominent glutamate receptor-mediated excitotoxicity that occurs after QA- (Mueller et al., 2005) and HI-induced brain injury (Martin, Brambrink, Lehmann, et al., 1997). It will be important to determine if

these astrocyte changes can be blocked pharmacologically by systemic administration of glutamate receptor antagonists. Higher FA also correlated with more normal neurons with perisomatic astrocyte GLT-1+ processes. Though these appositions must be examined by electron microscopy (Furuta et al., 1997), the astrocytes were presumably involved in glutamate reuptake to reduce the risk of neuronal death. Interestingly, neither DTI scalar was related to dying neurons with degenerating nuclear chromatin and GLT-1 cytoplasmic enrichment (Martin, Brambrink, Lehmann, et al., 1997).

Thus, swelling in astrocytes that regulate brain water and glutamate reuptake are associated with changes in FA. The physiology driving the fluid shift to astrocytes requires further study. The excitotoxicity and excessive astrocyte NMDA receptor activation (Verkhratsky & Kirchhoff, 2007) could cause cation influx into astrocytes with swelling (Choi, 1992). Alternatively, astrocyte swelling may indirectly influence FA or be a downstream result of other cellular processes that determine FA. Because astrocyte processes project without preferential orientation, they may not contribute to the baseline FA within a voxel. However, somal swelling could reduce intracellular restriction of three-dimensional water movement and dilute the FA from axonal tracts due to partial volume effects. The correlation between swollen astrocytes and FA could be secondary to anisotropy dilution rather than anisotropic changes within the astrocytes themselves.

4.2. White matter

FA is often used to measure white matter injury (Herbert et al., 2018). We used CNPase and BIN1 to immunophenotype oligodendrocyte cytopathology. CNPase levels are highest in oligodendrocytes, including oligodendrocyte progenitors and oligodendrocytes that produce myelin, relative to other neural cells (Lindberg et al., 2009; Radtke et al., 2011; Verrier et al., 2013). BIN1 identifies mature, myelinating oligodendrocytes (De Rossi et al., 2016; Lee, Santos, et al., 2020b). We found that degenerating oligodendrocytes had disrupted nuclear BIN1 enrichment (D'Alessandro et al., 2015) with BIN1 extrusion into the cytoplasm and nuclear vacuoles (Figure 10).

Lower FA correlated with more myelin process swellings in the internal capsule and with lower myelin density in the internal capsule and striatal white matter bundles. This is consistent with disrupted white matter microstructural organization among the myelin sheaths and axons. In caudate and putamen where myelin sheaths wrap neuronal processes, higher FA was associated with more normal CNPase+ oligodendrocytes, including recently replicated doublet cells, as an indicator of healthy white matter. The association between more apoptotic CNPase+ and BIN1+ cells with lower FA corroborated these findings.

MD was only related to the degeneration of myelinating oligodendrocytes in the internal capsule. Oligodendrocytes express glutamate receptors and are vulnerable to excitoxicity (Furuta & Martin, 1999). MD is sensitive to cellular necrosis with cell membrane breakdown, lysis, and decreased tortuosity with hindered water diffusion (Alexander et al., 2007; Lee, Liu, et al., 2020; Ranzenberger & Snyder, 2020). Our data show that microscopic oligodendrocyte degeneration in large white matter bundles is associated with MD in neonatal brain. It must be noted, however, that though we found statistically significant relationships between DTI and the oligodendrocyte and myelin measures, visual inspection

of the data showed possible outlier effects. In contrast, the astrocyte data showed stronger and more consistent correlations with FA.

4.3. Limitations

Our study had a small sample size and was descriptive. Future studies will include more HI piglets. We did not examine molecular injury mechanisms, though we do know that QA-induced excitotoxicity drives glial pathobiology. We did not assess axonal damage because the QA model is classically axon-sparing acutely (Schwarcz et al., 1984). Accordingly, we did not observe obvious neuropathological axonal swellings. We also did not use electron microscopy.

We studied a single ROI that encompassed internal capsule, putamen, and caudate because 3T MRI could not distinguish the internal capsule fascicles from intervening isthmi of gray matter in piglet brain. Accurate delineation of the white matter bundles requires higher resolution MRI. Edema may have influenced the in vivo MRI in addition to microstructural perturbations. Because our prior work showed that T2 did not differ in this cohort (Lee, Liu, et al., 2020), we did not analyze T2 MRI. All piglets were anesthetized and did not move during MRI though they were mechanically ventilated. Future imaging will include corrections for motion, geometrical distortion, and eddy current. We will also recover piglets for longer to study how evolving injury affects DTI (Tuor et al., 2014) and whether DTI predicts neurocognitive outcomes (Singh et al., 2019).

4.4. Conclusions

In neonatal piglets with excitotoxic and HI brain injury, astrocyte cytotoxic swelling is associated with abnormal FA alongside oligodendrocyte apoptosis and myelin process swelling. MD correlated with degeneration and loss of normal glia but not with the morphologic changes that accompany astrocyte or myelin process swelling. Our study provides a cytological interpretation for neonatal DTI at the microscopic level.

Acknowledgments.

We thank Claire Levine, MS, ESL, for her editorial assistance.

Funding. This study was supported by grants from the National Institutes of Health (R01 NS107417 [JKL, LJM, RCK]; R01 NS109029 [PL, JKL, RCK]; and R01 NS113921 [JKL, LJM, RCK]).

References

Abe Y, Takata N, Sakai Y, Hamada HT, Hiraoka Y, Aida T, Tanaka K, Bihan DL, Doya K, & Tanaka KF (2020, 9 1). Diffusion functional MRI reveals global brain network functional abnormalities driven by targeted local activity in a neuropsychiatric disease mouse model. Neuroimage, 223, 117318. 10.1016/j.neuroimage.2020.117318 [PubMed: 32882386]

Alexander AL, Lee JE, Lazar M, & Field AS (2007, 7). Diffusion tensor imaging of the brain. Neurotherapeutics, 4(3), 316–329. 10.1016/j.nurt.2007.05.011 [PubMed: 17599699]

Ancora G, Testa C, Grandi S, Tonon C, Sbravati F, Savini S, Manners DN, Gramegna LL, Tani G, Malucelli E, Corvaglia LT, Faldella G, & Lodi R (2013, 8). Prognostic value of brain proton MR spectroscopy and diffusion tensor imaging in newborns with hypoxic-ischemic encephalopathy treated by brain cooling. Neuroradiology, 55(8), 1017–1025. 10.1007/s00234-013-1202-5 [PubMed: 23703033]

Borsani E, Della Vedova AM, Rezzani R, Rodella LF, & Cristini C (2019, 3). Correlation between human nervous system development and acquisition of fetal skills: An overview. Brain and Development, 41(3), 225–233. 10.1016/j.braindev.2018.10.009 [PubMed: 30389271]

Bozek J, Makropoulos A, Schuh A, Fitzgibbon S, Wright R, Glasser MF, Coalson TS, O'Muircheartaigh J, Hutter J, Price AN, Cordero-Grande L, Teixeira R, Hughes E, Tusor N, Baruteau KP, Rutherford MA, Edwards AD, Hajnal JV, Smith SM, Rueckert D, Jenkinson M, & Robinson EC (2018, 10 1). Construction of a neonatal cortical surface atlas using Multimodal Surface Matching in the Developing Human Connectome Project. Neuroimage, 179, 11–29. 10.1016/j.neuroimage.2018.06.018 [PubMed: 29890325]

Brissaud O, Amirault M, Villega F, Periot O, Chateil JF, & Allard M (2010, 2). Efficiency of fractional anisotropy and apparent diffusion coefficient on diffusion tensor imaging in prognosis of neonates with hypoxic-ischemic encephalopathy: a methodologic prospective pilot study. AJNR: American Journal of Neuroradiology, 31(2), 282–287. 10.3174/ajnr.A1805 [PubMed: 19959775]

Bylicky MA, Mueller GP, & Day RM (2018). Mechanisms of Endogenous Neuroprotective Effects of Astrocytes in Brain Injury. Oxidative Medicine and Cellular Longevity, 2018, 6501031. 10.1155/2018/6501031 [PubMed: 29805731]

Carrasco M, Perin J, Jennings JM, Parkinson C, Gilmore MM, Chavez-Valdez R, Massaro AN, Koehler RC, Northington FJ, Tekes A, & Lee JK (2018, 5). Cerebral Autoregulation and Conventional and Diffusion Tensor Imaging Magnetic Resonance Imaging in Neonatal Hypoxic-Ischemic Encephalopathy. Pediatric Neurology, 82, 36–43. 10.1016/j.pediatrneurol.2018.02.004 [PubMed: 29622488]

Choi DW (1992, 11). Excitotoxic cell death. Journal of Neurobiology, 23(9), 1261–1276. 10.1002/neu.480230915 [PubMed: 1361523]

D'Alessandro M, Hnia K, Gache V, Koch C, Gavriilidis C, Rodriguez D, Nicot AS, Romero NB, Schwab Y, Gomes E, Labouesse M, & Laporte J (2015, 10 26). Amphiphysin 2 Orchestrates Nucleus Positioning and Shape by Linking the Nuclear Envelope to the Actin and Microtubule Cytoskeleton. Developmental Cell, 35(2), 186–198. 10.1016/j.devcel.2015.09.018 [PubMed: 26506308]

de Graaf-Peters VB, & Hadders-Algra M (2006, 4). Ontogeny of the human central nervous system: what is happening when? Early Human Development, 82(4), 257–266. 10.1016/j.earlhumdev.2005.10.013 [PubMed: 16360292]

De Rossi P, Buggia-Prevot V, Clayton BL, Vasquez JB, van Sanford C, Andrew RJ, Lesnick R, Botte A, Deyts C, Salem S, Rao E, Rice RC, Parent A, Kar S, Popko B, Pytel P, Estus S, & Thinakaran G (2016, 8 3). Predominant expression of Alzheimer's disease-associated BIN1 in mature oligodendrocytes and localization to white matter tracts. Molecular Neurodegeneration, 11(1), 59. 10.1186/s13024-016-0124-1 [PubMed: 27488240]

Debacker C, Djemai B, Ciobanu L, Tsurugizawa T, & Le Bihan D (2020). Diffusion MRI reveals in vivo and non-invasively changes in astrocyte function induced by an aquaporin-4 inhibitor. PloS One, 15(5), e0229702. 10.1371/journal.pone.0229702 [PubMed: 32413082]

Dobbing J, & Sands J (1979, 3). Comparative aspects of the brain growth spurt. Early Human Development, 3(1), 79–83. 10.1016/0378-3782(79)90022-7 [PubMed: 118862]

Farrell JA, Landman BA, Jones CK, Smith SA, Prince JL, van Zijl PC, & Mori S (2007, 9). Effects of signal-to-noise ratio on the accuracy and reproducibility of diffusion tensor imaging-derived fractional anisotropy, mean diffusivity, and principal eigenvector measurements at 1.5 T. Journal of Magnetic Resonance Imaging, 26(3), 756–767. 10.1002/jmri.21053 [PubMed: 17729339]

Furuta A, & Martin LJ (1999, 4). Laminar segregation of the cortical plate during corticogenesis is accompanied by changes in glutamate receptor expression. Journal of Neurobiology, 39(1), 67–80. 10.1002/(Sici)1097-4695(199904)39:1<67::Aid-Neu6>3.0.Co;2-7 [PubMed: 10213454]

Furuta A, Rothstein JD, & Martin LJ (1997, 11 1). Glutamate transporter protein subtypes are expressed differentially during rat CNS development. Journal of Neuroscience, 17(21), 8363–8375. 10.1523/jneurosci.17-21-08363.1997 [PubMed: 9334410]

Ginsberg SD, Rothstein JD, Price DL, & Martin LJ (1996, 9). Fimbria-fornix transections selectively down-regulate subtypes of glutamate transporter and glutamate receptor proteins in septum and hippocampus. Journal of Neurochemistry, 67(3), 1208–1216. 10.1046/j.1471-4159.1996.67031208.x [PubMed: 8752128]

Hama K, Arii T, Katayama E, Marton M, & Ellisman MH (2004, 5). Tri-dimensional morphometric analysis of astrocytic processes with high voltage electron microscopy of thick Golgi preparations. Journal of Neurocytology, 33(3), 277–285. 10.1023/B:NEUR.0000044189.08240.a2 [PubMed: 15475683]

Herbert E, Engel-Hills P, Hattingh C, Fouche JP, Kidd M, Lochner C, Kotze MJ, & van Rensburg SJ (2018, 4). Fractional anisotropy of white matter, disability and blood iron parameters in multiple sclerosis. Metabolic Brain Disease, 33(2), 545–557. 10.1007/s11011-017-0171-5 [PubMed: 29396631]

Herculano-Houzel S (2014, 9). The glia/neuron ratio: how it varies uniformly across brain structures and species and what that means for brain physiology and evolution. Glia, 62(9), 1377–1391. 10.1002/glia.22683 [PubMed: 24807023]

Ishibashi N, Scafidi J, Murata A, Korotcova L, Zurakowski D, Gallo V, & Jonas RA (2012, 2 21). White matter protection in congenital heart surgery. Circulation, 125(7), 859–871. 10.1161/CIRCULATIONAHA.111.048215 [PubMed: 22247493]

Jablonski EM, Webb AN, McConnell NA, Riley MC, & Hughes FM Jr. (2004, 4). Plasma membrane aquaporin activity can affect the rate of apoptosis but is inhibited after apoptotic volume decrease. American Journal of Physiology: Cell Physiology, 286(4), C975–985. 10.1152/ajpcell.00180.2003 [PubMed: 14644770]

Johnston MV (2001). Excitotoxicity in neonatal hypoxia. Ment Retard Dev Disabil Res Rev, 7(4), 229–234. 10.1002/mrdd.1032 [PubMed: 11754516]

Johnston MV (2005, 7). Excitotoxicity in perinatal brain injury. Brain Pathology, 15(3), 234–240. 10.1111/j.1750-3639.2005.tb00526.x [PubMed: 16196390]

Koehler RC, Yang ZJ, Lee JK, & Martin LJ (2018, 12). Perinatal hypoxic-ischemic brain injury in large animal models: Relevance to human neonatal encephalopathy. Journal of Cerebral Blood Flow and Metabolism, 38(12), 2092–2111. 10.1177/0271678X18797328 [PubMed: 30149778]

Larson AC, Jamrogowicz JL, Kulikowicz E, Wang B, Yang ZJ, Shaffner DH, Koehler RC, & Lee JK (2013, 11). Cerebrovascular autoregulation after rewarming from hypothermia in a neonatal swine model of asphyxic brain injury. J Appl Physiol (1985), 115(10), 1433–1442. 10.1152/japplphysiol.00238.2013 [PubMed: 24009008]

Lawn J, Shibuya K, & Stein C (2005, 6). No cry at birth: global estimates of intrapartum stillbirths and intrapartum-related neonatal deaths. Bulletin of the World Health Organization, 83(6), 409–417. https://doi.org/S0042-96862005000600008 [pii] [PubMed: 15976891]

Lee JK, Liu D, Raven EP, Jiang D, Liu P, Qin Q, Kulikowicz E, Santos PT, Adams S, Zhang J, Koehler RC, Martin LJ, & Tekes A (2020, 10). Mean Diffusivity in Striatum Correlates With Acute Neuronal Death but Not Lesser Neuronal Injury in a Pilot Study of Neonatal Piglets With Encephalopathy. Journal of Magnetic Resonance Imaging, 52(4), 1216–1226. 10.1002/jmri.27181 [PubMed: 32396711]

Lee JK, Poretti A, Perin J, Huisman T, Parkinson C, Chavez-Valdez R, O'Connor M, Reyes M, Armstrong J, Jennings JM, Gilmore MM, Koehler RC, Northington FJ, & Tekes A (2017). Optimizing Cerebral Autoregulation May Decrease Neonatal Regional Hypoxic-Ischemic Brain Injury. Developmental Neuroscience, 39(1–4), 248–256. 10.1159/000452833 [PubMed: 27978510]

Lee JK, Santos PT, Chen MW, O'Brien CE, Kulikowicz E, Adams S, Hardart H, Koehler RC, & Martin LJ (2020a, 11 19). Combining Hypothermia and Oleuropein Subacutely Protects Subcortical White Matter in a Swine Model of Neonatal Hypoxic-Ischemic Encephalopathy. Journal of Neuropathology and Experimental Neurology. 10.1093/jnen/nlaa132

Lee JK, Santos PT, Chen MW, O'Brien CE, Kulikowicz E, Adams S, Hardart H, Koehler RC, & Martin LJ (2020b). Combining hypothermia and oleuropein subacutely protects subcortical white matter in a swine model of neonatal hypoxic-ischemic encephalopathy. Journal of Neuropathology and Experimental Neurology, In print. 10.1093/jnen/nlaa132

Lee JK, Wang B, Reyes M, Armstrong JS, Kulikowicz E, Santos PT, Lee JH, Koehler RC, & Martin LJ (2016). Hypothermia and Rewarming Activate a Macroglial Unfolded Protein Response Independent of Hypoxic-Ischemic Brain Injury in Neonatal Piglets. Developmental Neuroscience, 38(4), 277–294. 10.1159/000448585 [PubMed: 27622292]

Lesuisse C, & Martin LJ (2002, 4). Long-term culture of mouse cortical neurons as a model for neuronal development, aging, and death. Journal of Neurobiology, 51(1), 9–23. 10.1002/neu.10037 [PubMed: 11920724]

Lindberg N, Kastemar M, Olofsson T, Smits A, & Uhrbom L (2009, 6 11). Oligodendrocyte progenitor cells can act as cell of origin for experimental glioma. Oncogene, 28(23), 2266–2275. 10.1038/onc.2009.76 [PubMed: 19421151]

Liu L, Johnson HL, Cousens S, Perin J, Scott S, Lawn JE, Rudan I, Campbell H, Cibulskis R, Li M, Mathers C, Black RE, Child Health Epidemiology Reference Group of, W. H. O., & Unicef. (2012). Global, regional, and national causes of child mortality: an updated systematic analysis for 2010 with time trends since 2000. Lancet (London, England), 379(9832), 2151–2161. 10.1016/S0140-6736(12)60560-1 [doi]

Lodygensky GA, West T, Moravec MD, Back SA, Dikranian K, Holtzman DM, & Neil JJ (2011, 9). Diffusion characteristics associated with neuronal injury and glial activation following hypoxia-ischemia in the immature brain. Magnetic Resonance in Medicine, 66(3), 839–845. 10.1002/mrm.22869 [PubMed: 21394776]

Lucke AM, Shetty AN, Hagan JL, Walton A, Stafford TD, Chu ZD, Rhee CJ, Kaiser JR, & Sanz Cortes M (2019, 6). Early proton magnetic resonance spectroscopy during and after therapeutic hypothermia in perinatal hypoxic-ischemic encephalopathy. Pediatric Radiology, 49(7), 941–950. 10.1007/s00247-019-04383-8 [PubMed: 30918993]

Lugo-Huitrón R, Ugalde Muñiz P, Pineda B, Pedraza-Chaverrí J, Ríos C, & Pérez-de la Cruz V (2013). Quinolinic acid: an endogenous neurotoxin with multiple targets. Oxidative Medicine and Cellular Longevity, 2013, 104024. 10.1155/2013/104024 [PubMed: 24089628]

Maas LC, Mukherjee P, Carballido-Gamio J, Veeraraghavan S, Miller SP, Partridge SC, Henry RG, Barkovich AJ, & Vigneron DB (2004, 7). Early laminar organization of the human cerebrum demonstrated with diffusion tensor imaging in extremely premature infants. Neuroimage, 22(3), 1134–1140. 10.1016/j.neuroimage.2004.02.035 [PubMed: 15219585]

Martin LJ, Al-Abdulla NA, Brambrink AM, Kirsch JR, Sieber FE, & Portera-Cailliau C (1998, 7 1). Neurodegeneration in excitotoxicity, global cerebral ischemia, and target deprivation: A perspective on the contributions of apoptosis and necrosis. Brain Research Bulletin, 46(4), 281–309. 10.1016/s0361-9230(98)00024-0 [PubMed: 9671259]

Martin LJ, Brambrink A, Koehler RC, & Traystman RJ (1997, 1 13). Primary sensory and forebrain motor systems in the newborn brain are preferentially damaged by hypoxia-ischemia. Journal of Comparative Neurology, 377(2), 262–285. 10.1002/(sici)1096-9861(19970113)377:2<262::aid-cne8>3.0.co;2-1

Martin LJ, Brambrink AM, Lehmann C, Portera-Cailliau C, Koehler R, Rothstein J, & Traystman RJ (1997, 9). Hypoxia-ischemia causes abnormalities in glutamate transporters and death of astroglia and neurons in newborn striatum. Annals of Neurology, 42(3), 335–348. 10.1002/ana.410420310 [PubMed: 9307255]

Martin LJ, Doebler JA, & Anthony A (1986, 1). Cytophotometric analysis of neuronal chromatin and RNA changes in oxotremorine-treated rats. Proceedings of the Society for Experimental Biology and Medicine, 181(1), 41–48. 10.3181/00379727-181-42222 [PubMed: 2418445]

Martin LJ, Hadfield MG, Dellovade TL, & Price DL (1991). The striatal mosaic in primates: patterns of neuropeptide immunoreactivity differentiate the ventral striatum from the dorsal striatum. Neuroscience, 43(2–3), 397–417. 10.1016/0306-4522(91)90303-6 [PubMed: 1681464]

Martin LJ, & Wong M (2013, 10). Aberrant regulation of DNA methylation in amyotrophic lateral sclerosis: a new target of disease mechanisms. Neurotherapeutics, 10(4), 722–733. 10.1007/s13311-013-0205-6 [PubMed: 23900692]

Mori S, & Zhang J (2006, 9 7). Principles of diffusion tensor imaging and its applications to basic neuroscience research. Neuron, 51(5), 527–539. 10.1016/j.neuron.2006.08.012 [PubMed: 16950152]

Mudd AT, & Dilger RN (2017, 1). Early-Life Nutrition and Neurodevelopment: Use of the Piglet as a Translational Model. Advances in Nutrition, 8(1), 92–104. 10.3945/an.116.013243 [PubMed: 28096130]

Mueller D, Shamblott MJ, Fox HE, Gearhart JD, & Martin LJ (2005, 12 1). Transplanted human embryonic germ cell-derived neural stem cells replace neurons and oligodendrocytes in the

forebrain of neonatal mice with excitotoxic brain damage. Journal of Neuroscience Research, 82(5), 592–608. 10.1002/jnr.20673 [PubMed: 16247803]

Mukherjee A, Wu D, Davis HC, & Shapiro MG (2016, 12 23). Non-invasive imaging using reporter genes altering cellular water permeability. Nat Commun, 7, 13891. 10.1038/ncomms13891 [PubMed: 28008959]

Muns R, Manzanilla EG, Sol C, Manteca X, & Gasa J (2013, 4). Piglet behavior as a measure of vitality and its influence on piglet survival and growth during lactation. Journal of Animal Science, 91(4), 1838–1843. 10.2527/jas.2012-5501 [PubMed: 23408816]

Neil JJ, Shiran SI, McKinstry RC, Schefft GL, Snyder AZ, Almli CR, Akbudak E, Aronovitz JA, Miller JP, Lee BC, & Conturo TE (1998, 10). Normal brain in human newborns: apparent diffusion coefficient and diffusion anisotropy measured by using diffusion tensor MR imaging. Radiology, 209(1), 57–66. 10.1148/radiology.209.1.9769812 [PubMed: 9769812]

Northington FJ, Traystman RJ, Koehler RC, & Martin LJ (1999, 6 15). GLT1, glial glutamate transporter, is transiently expressed in neurons and develops astrocyte specificity only after midgestation in the ovine fetal brain. Journal of Neurobiology, 39(4), 515–526. [PubMed: 10380073]

Northington FJ, Traystman RJ, Koehler RC, Rothstein JD, & Martin LJ (1998, 8). Regional and cellular expression of glial (GLT1) and neuronal (EAAC1) glutamate transporter proteins in ovine fetal brain. Neuroscience, 85(4), 1183–1194. 10.1016/s0306-4522(97)00673-8 [PubMed: 9681956]

Oberheim NA, Takano T, Han X, He W, Lin JH, Wang F, Xu Q, Wyatt JD, Pilcher W, Ojemann JG, Ransom BR, Goldman SA, & Nedergaard M (2009, 3 11). Uniquely hominid features of adult human astrocytes. Journal of Neuroscience, 29(10), 3276–3287. 10.1523/JNEUROSCI.4707-08.2009 [PubMed: 19279265]

Oishi K, Faria AV, & Mori S (2012, 2). Advanced neonatal NeuroMRI. Magnetic Resonance Imaging Clinics of North America, 20(1), 81–91. 10.1016/j.mric.2011.08.009 [PubMed: 22118594]

Panzardi A, Bernardi ML, Mellagi AP, Bierhals T, Bortolozzo FP, & Wentz I (2013, 6 1). Newborn piglet traits associated with survival and growth performance until weaning. Preventive Veterinary Medicine, 110(2), 206–213. 10.1016/j.prevetmed.2012.11.016 [PubMed: 23237812]

Portera-Cailliau C, Price DL, & Martin LJ (1997, 2 3). Non-NMDA and NMDA receptor-mediated excitotoxic neuronal deaths in adult brain are morphologically distinct: further evidence for an apoptosis-necrosis continuum. Journal of Comparative Neurology, 378(1), 88–104. https://www.ncbi.nlm.nih.gov/pubmed/9120056

Potokar M, Jorgačevski J, & Zorec R (2016, 7 13). Astrocyte Aquaporin Dynamics in Health and Disease. International Journal of Molecular Sciences, 17(7). 10.3390/ijms17071121

Radtke C, Sasaki M, Lankford KL, Gallo V, & Kocsis JD (2011). CNPase expression in olfactory ensheathing cells. Journal of Biomedicine & Biotechnology, 2011, 608496. 10.1155/2011/608496 [PubMed: 22174557]

Ranzenberger LR, & Snyder T (2020). Diffusion Tensor Imaging. In StatPearls. StatPearls Publishing Copyright © 2020, StatPearls Publishing LLC.

Rodriguez-Grande B, Obenaus A, Ichkova A, Aussudre J, Bessy T, Barse E, Hiba B, Catheline G, Barrière G, & Badaut J (2018, 8). Gliovascular changes precede white matter damage and long-term disorders in juvenile mild closed head injury. Glia, 66(8), 1663–1677. 10.1002/glia.23336 [PubMed: 29665077]

Rose CR, & Kirchhoff F (2015). Glial heterogeneity: the increasing complexity of the brain [Editorial]. e-Neuroforum, 6, 59–62. 10.1007/s13295-015-0012-0

Rosito S, Nicchia GP, Palazzo C, Lia A, Buccoliero C, Pisani F, Svelto M, Trojano M, & Frigeri A (2018, 2). Supramolecular aggregation of aquaporin-4 is different in muscle and brain: correlation with tissue susceptibility in neuromyelitis optica. Journal of Cellular and Molecular Medicine, 22(2), 1236–1246. 10.1111/jcmm.13401 [PubMed: 29055082]

Saha S, Pagnozzi A, Bourgeat P, George JM, Bradford D, Colditz PB, Boyd RN, Rose SE, Fripp J, & Pannek K (2020, 7 15). Predicting motor outcome in preterm infants from very early brain diffusion MRI using a deep learning convolutional neural network (CNN) model. Neuroimage, 215, 116807. 10.1016/j.neuroimage.2020.116807 [PubMed: 32278897]

Santos PT, O'Brien CE, Chen MW, Hopkins CD, Adams S, Kulikowicz E, Singh R, Koehler RC, Martin LJ, & Lee JK (2018, 10 16). Proteasome Biology Is Compromised in White Matter After Asphyxic Cardiac Arrest in Neonatal Piglets. J Am Heart Assoc, 7(20), e009415. 10.1161/JAHA.118.009415 [PubMed: 30371275]

Schwarcz R, Foster AC, French ED, Whetsell WO Jr., & Köhler C (1984, 7 2). Excitotoxic models for neurodegenerative disorders. Life Sciences, 35(1), 19–32. 10.1016/0024-3205(84)90148-6 [PubMed: 6234446]

Sheng HZ, Kerlero de Rosbo N, Carnegie PR, & Bernard CC (1989, 3). Developmental study of myelin basic protein variants in various regions of pig nervous system. Journal of Neurochemistry, 52(3), 736–740. 10.1111/j.1471-4159.1989.tb02516.x [PubMed: 2465378]

Shetty AN, Lucke AM, Liu P, Sanz Cortes M, Hagan JL, Chu ZD, Hunter JV, Lu H, Lee W, & Kaiser JR (2019, 2). Cerebral oxygen metabolism during and after therapeutic hypothermia in neonatal hypoxic-ischemic encephalopathy: a feasibility study using magnetic resonance imaging. Pediatric Radiology, 49(2), 224–233. 10.1007/s00247-018-4283-9 [PubMed: 30402807]

Simchick G, Shen A, Campbell B, Park HJ, West FD, & Zhao Q (2019, 9). Pig Brains Have Homologous Resting-State Networks with Human Brains. Brain Connectivity, 9(7), 566–579. 10.1089/brain.2019.0673 [PubMed: 31115245]

Singh R, Kulikowicz E, Santos PT, Koehler RC, Martin LJ, & Lee JK (2019, 9 2). Spatial T-maze identifies cognitive deficits in piglets 1 month after hypoxia-ischemia in a model of hippocampal pyramidal neuron loss and interneuron attrition. Behavioural Brain Research, 369, 111921. 10.1016/j.bbr.2019.111921 [PubMed: 31009645]

Siu CR, Balsor JL, Jones DG, & Murphy KM (2015). Classic and Golli Myelin Basic Protein have distinct developmental trajectories in human visual cortex. Frontiers in Neuroscience, 9, 138. 10.3389/fnins.2015.00138 [PubMed: 25964736]

Sweasey D, Patterson DS, & Glancy EM (1976, 8). Biphasic myelination and the fatty acid composition of cerebrosides and cholesterol esters in the developing central nervous system of the domestic pig. Journal of Neurochemistry, 27(2), 375–380. 10.1111/j.1471-4159.1976.tb12256.x [PubMed: 965978]

Tekes A, Poretti A, Scheurkogel MM, Huisman TA, Howlett JA, Alqahtani E, Lee JH, Parkinson C, Shapiro K, Chung SE, Jennings JM, Gilmore MM, Hogue CW, Martin LJ, Koehler RC, Northington FJ, & Lee JK (2015, 1). Apparent diffusion coefficient scalars correlate with near-infrared spectroscopy markers of cerebrovascular autoregulation in neonates cooled for perinatal hypoxic-ischemic injury. AJNR: American Journal of Neuroradiology, 36(1), 188–193. 10.3174/ajnr.A4083 [PubMed: 25169927]

Tomás-Camardiel M, Venero JL, de Pablos RM, Rite I, Machado A, & Cano J (2004, 11). In vivo expression of aquaporin-4 by reactive microglia. Journal of Neurochemistry, 91(4), 891–899. 10.1111/j.1471-4159.2004.02759.x [PubMed: 15525343]

Tuor UI, Morgunov M, Sule M, Qiao M, Clark D, Rushforth D, Foniok T, & Kirton A (2014). Cellular correlates of longitudinal diffusion tensor imaging of axonal degeneration following hypoxic-ischemic cerebral infarction in neonatal rats. Neuroimage Clin, 6, 32–42. 10.1016/j.nicl.2014.08.003 [PubMed: 25379414]

van der Toorn A, Sykova E, Dijkhuizen RM, Vorisek I, Vargova L, Skobisova E, van Lookeren Campagne M, Reese T, & Nicolay K (1996, 7). Dynamic changes in water ADC, energy metabolism, extracellular space volume, and tortuosity in neonatal rat brain during global ischemia. Magnetic Resonance in Medicine, 36(1), 52–60. 10.1002/mrm.1910360110 [PubMed: 8795020]

Van Essen DC, Smith SM, Barch DM, Behrens TE, Yacoub E, Ugurbil K, & Consortium WU-MH (2013, 10 15). The WU-Minn Human Connectome Project: an overview. Neuroimage, 80, 62–79. 10.1016/j.neuroimage.2013.05.041 [PubMed: 23684880]

Verkhratsky A, & Kirchhoff F (2007, 2). NMDA Receptors in glia. Neuroscientist, 13(1), 28–37. 10.1177/1073858406294270 [PubMed: 17229973]

Verrier JD, Jackson TC, Gillespie DG, Janesko-Feldman K, Bansal R, Goebbels S, Nave KA, Kochanek PM, & Jackson EK (2013, 10). Role of CNPase in the oligodendrocytic extracellular 2',3'-cAMP-adenosine pathway. Glia, 61(10), 1595–1606. 10.1002/glia.22523 [PubMed: 23922219]

von Bartheld CS, Bahney J, & Herculano-Houzel S (2016, 12 15). The search for true numbers of neurons and glial cells in the human brain: A review of 150 years of cell counting. Journal of Comparative Neurology, 524(18), 3865–3895. 10.1002/cne.24040

Wang B, Armstrong JS, Lee JH, Bhalala U, Kulikowicz E, Zhang H, Reyes M, Moy N, Spicer D, Zhu J, Yang ZJ, Koehler RC, Martin LJ, & Lee JK (2015, 5). Rewarming from therapeutic hypothermia induces cortical neuron apoptosis in a swine model of neonatal hypoxic-ischemic encephalopathy. Journal of Cerebral Blood Flow and Metabolism, 35(5), 781–793. 10.1038/jcbfm.2014.245 [PubMed: 25564240]

Wang B, Armstrong JS, Reyes M, Kulikowicz E, Lee JH, Spicer D, Bhalala U, Yang ZJ, Koehler RC, Martin LJ, & Lee JK (2016). White matter apoptosis is increased by delayed hypothermia and rewarming in a neonatal piglet model of hypoxic ischemic encephalopathy. Neuroscience, 316, 296–310. [PubMed: 26739327]

Warntjes JBM, Persson A, Berge J, & Zech W (2017, 6). Myelin Detection Using Rapid Quantitative MR Imaging Correlated to Macroscopically Registered Luxol Fast Blue-Stained Brain Specimens. *AJNR*: American Journal of Neuroradiology, 38(6), 1096–1102. 10.3174/ajnr.A5168 [PubMed: 28428209]

Yano R, Hata J, Abe Y, Seki F, Yoshida K, Komaki Y, Okano H, & Tanaka KF (2018, 10). Quantitative temporal changes in DTI values coupled with histological properties in cuprizone-induced demyelination and remyelination. Neurochemistry International, 119, 151–158. 10.1016/j.neuint.2017.10.004 [PubMed: 29030079]

Yuan W, Deren KE, McAllister JP 2nd, Holland SK, Lindquist DM, Cancelliere A, Mason M, Shereen A, Hertzler DA, Altaye M, & Mangano FT (2010, 11 5). Diffusion tensor imaging correlates with cytopathology in a rat model of neonatal hydrocephalus. Cerebrospinal Fluid Res, 7, 19. 10.1186/1743-8454-7-19 [PubMed: 21054844]

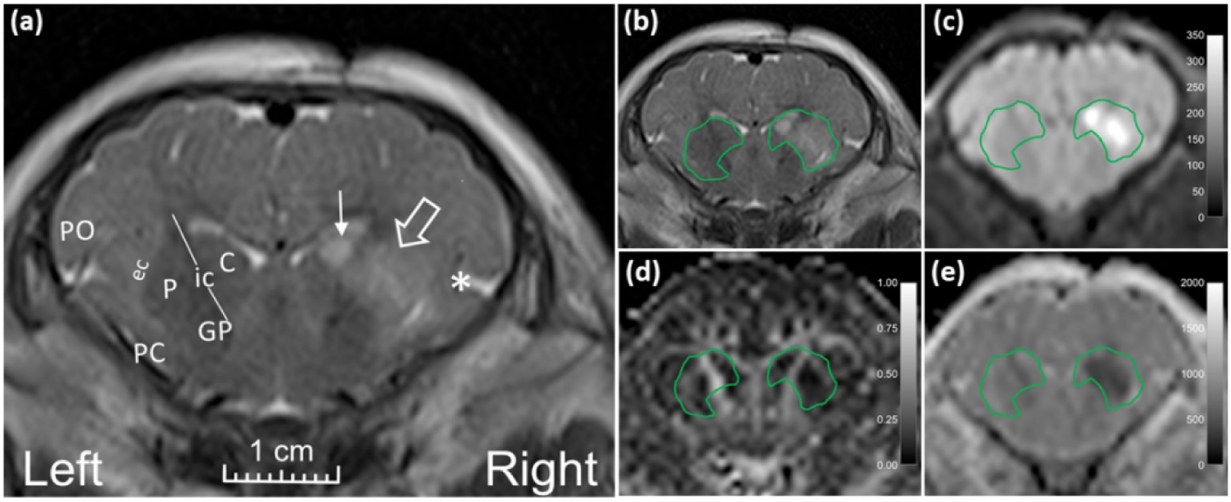

Figure 1.

Representative MR images from a neonatal piglet that received stereotaxic injections of quinolinic acid (QA; 960 nmol, right) and contralateral phosphate-buffered saline (PBS, control, left) with 24-h survival. **(a)** High signal in the putamen (open arrow), caudate (line arrow), and deep insular cortex (asterisk) on the QA-injected side is visible on the T2-weighted coronal image. Anatomic landmarks are shown in the PBS-injected side: P, putamen; C, caudate; ic, internal capsule; GP, globus pallidus; ec, external capsule; PC, piriform cortex; and PO, parietal operculum. Manually defined regions of interest (ROI) encompassing the putamen, internal capsule, and caudate in **(b)** T2-weighted and **(c)** diffusion-weighted images show increased signal from QA injury. **(d)** Fractional anisotropy and **(e)** mean diffusivity were measured in the ROIs containing putamen, internal capsule, and caudate.

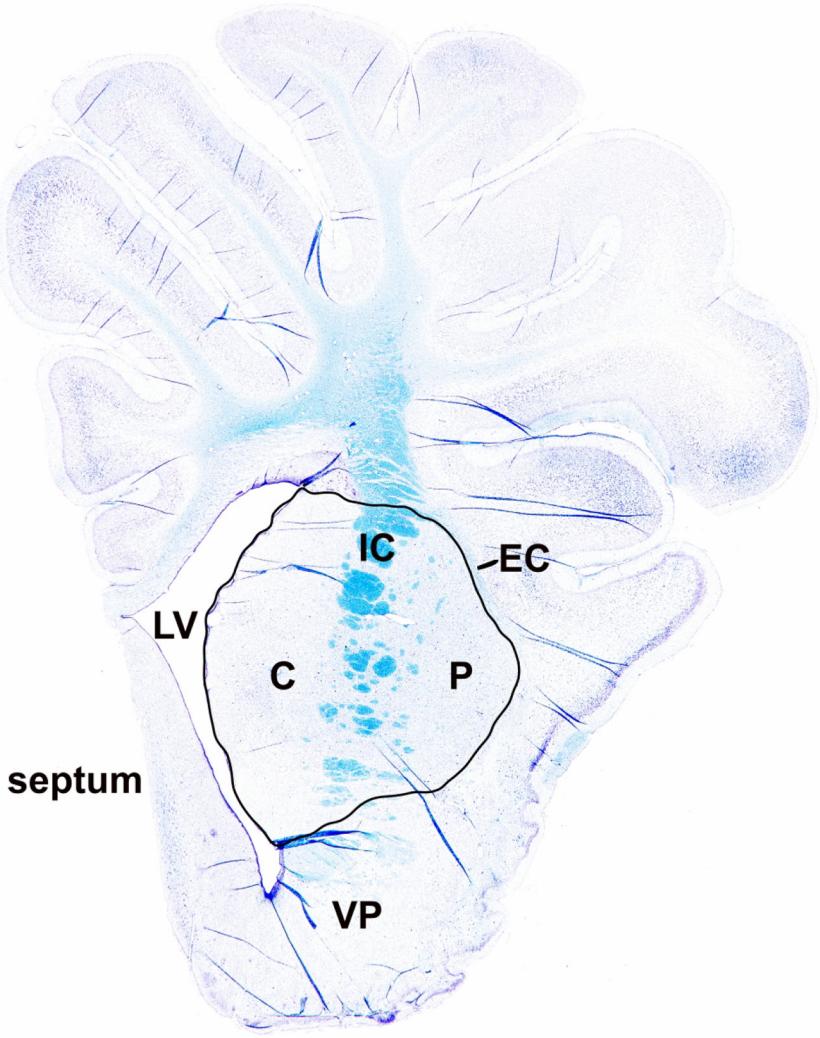

Figure 2.

Luxol fast blue staining of myelin. Greater myelin density stains darker azure (blue). In piglet brain, the internal capsule consists of discontinuous white matter bundles with intervening parcels of gray matter. Thus, at anterior levels, the internal capsule in piglet is a heterogeneous white matter-gray matter structure. Myelin density was measured in the region of interest encompassing caudate (C), internal capsule (IC), and putamen (P). The external capsule (EC), left ventricle (LV), septum, and ventral pallidum (VP) are also identified.

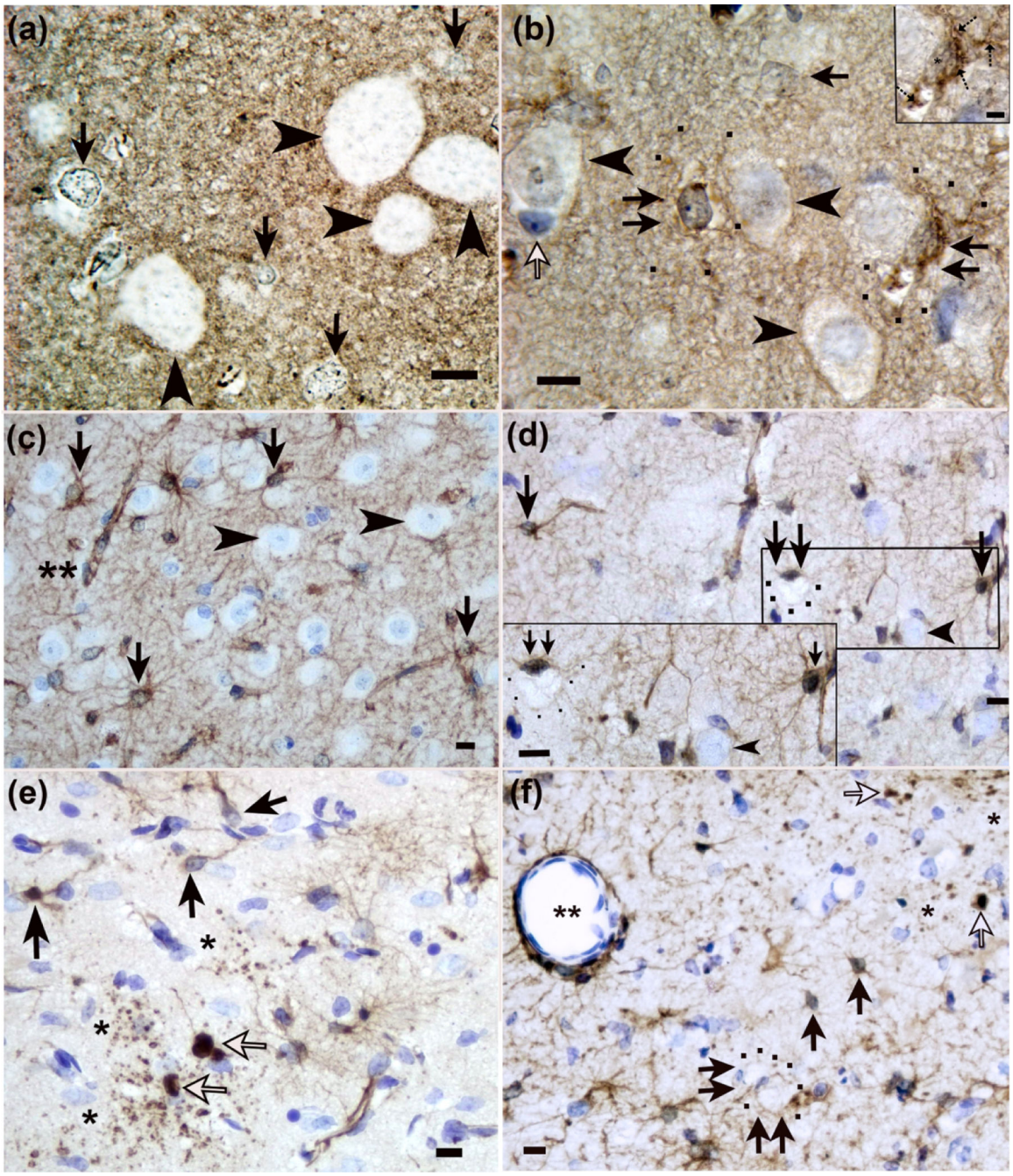

Figure 3.

Identification of astrocytes and astrocyte swelling in piglet encephalopathy using **(a, b)** aquaporin 4 (AQP4) and **(c-f)** glial fibrillary acidic protein (GFAP) immunohistochemistry. **(a)** A sham piglet had normal astrocytes with AQP4+ aggregates in the cell soma and nucleus but no prominent swelling (arrows) in putamen. The arrowheads show neurons. **(b)** Putamen of a piglet injected with 960 nmol quinolinic acid (QA) shows swollen astrocytes with AQP4+ aggregates, cytoplasmic swelling, and vacuoles (double arrows). The black dots outline AQP4-labeled distal processes of the enlarged astrocyte. The inset shows a swollen

astrocyte with prominent AQP4+ aggregates in the cell body and processes (hatched arrows), vacuoles, and an asterisk marking the nucleus. In the main panel, the single arrows show astrocytes without swelling (white arrow: AQP4-negative; black single arrow: AQP4+). Arrowheads show neurons. **(c)** GFAP staining in sham putamen showed normal astrocytes (arrows). Perivascular astrocyte labeling showed no apparent vasogenic edema (double asterisks). Arrowheads denote neurons. **(d)** After hypoxia-ischemia (HI), the caudate had GFAP+ swollen astrocytes (double arrows), and black dots outline the swollen astrocyte's soma. Single arrows show normal astrocytes. Neurons are marked by arrowheads. **(e)** Putamen of an HI piglet showed GFAP+ degenerating astrocytes (white arrows) with clasmatodendrosis (fragmentation of the astrocyte's processes; asterisks). Black arrows show normal astrocytes and processes. **(f)** Injection of 960 nmol QA caused degeneration of GFAP+ astrocytes (white arrows) with clasmatodendrosis (single asterisks). Double arrows show two swollen astrocytes with enlarged cell bodies that are outlined by black dots. This astrocyte swelling is consistent with cytotoxic edema. The double asterisks show a vessel with tight AQP4 astrocyte labeling against the vessel wall without apparent vasogenic edema. Single black arrows show normal astrocytes. Panels A, B, and inset D were photographed at 1000x with oil immersion. The main panels C-F were photographed at 400x. Scale bars=10 μm in all main panels and inset D. The scale bar in inset B is 5 μm.

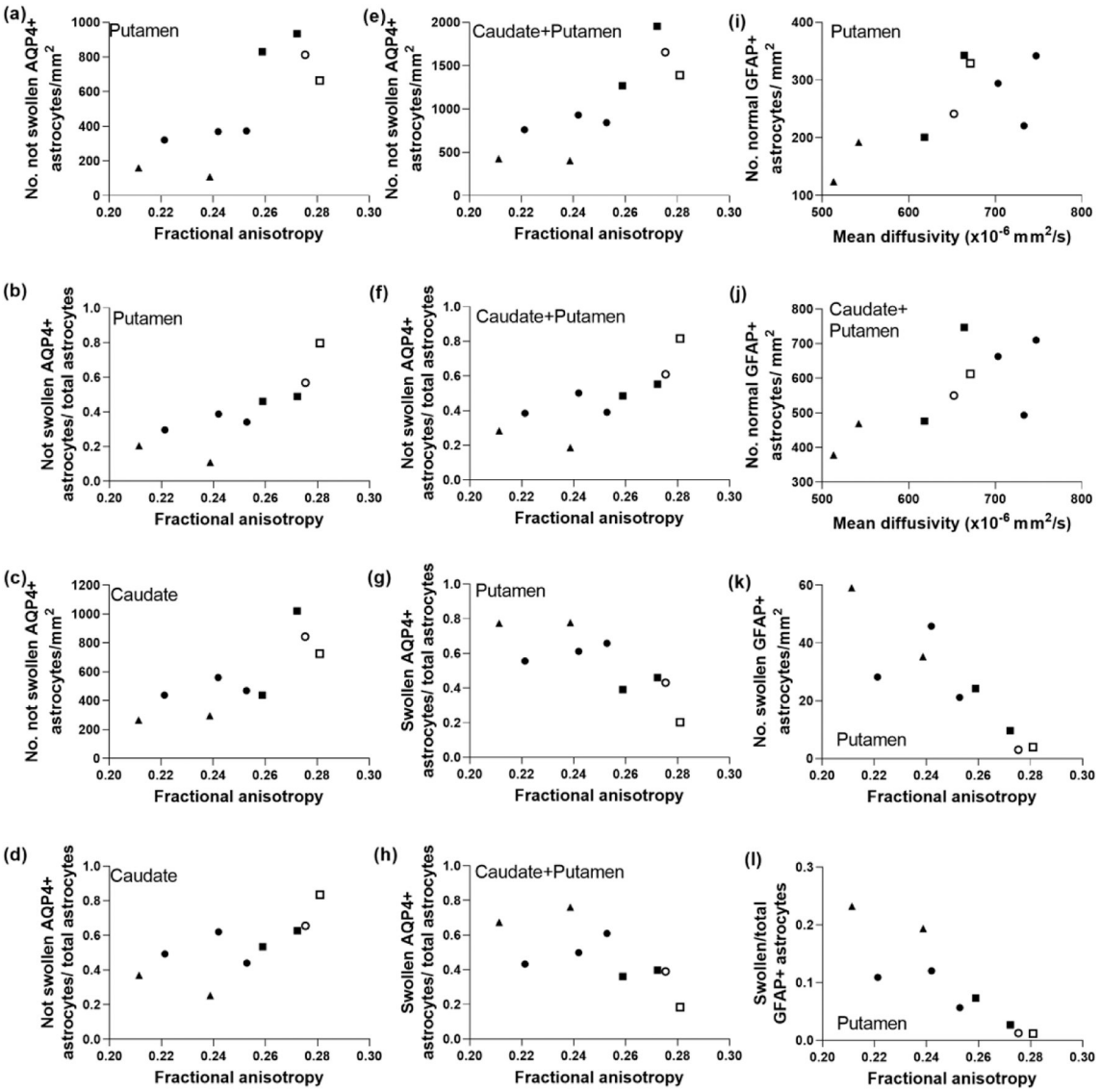

Figure 4.

The morphology and number of aquaporin 4 (AQP4)- and glial fibrillary acidic protein (GFAP)-labeled astrocytes correlated with diffusion tensor imaging in piglets with striatal encephalopathy. Astrocytes were classified as being positive or negative for AQP4 and as being swollen or not swollen. **(a, b)** In putamen, the number of AQP4+ astrocytes without swelling (r=0.800; p=0.014) and the ratio to total astrocytes (r=0.933; p=0.001) positively correlated with fractional anisotropy (FA). **(c, d)** Similar relationships were observed in caudate, as FA correlated with the number of non-swollen AQP4+ astrocytes (r=0.820; p=0.010) and with the ratio of non-swollen AQP4+ astrocytes to total astrocytes (r=0.850; p=0.006). **(e, f)** FA correlated with the sum counts of AQP4+ astrocytes without swelling in putamen and caudate (r=0.867; p=0.005) and the ratio (r=0.900; p=0.002). **(g)** The number of swollen AQP4+ astrocytes in putamen inversely correlated with FA (r= −0.800; p=0.014). **(h)** The ratio of swollen AQP4+ astrocytes to total astrocytes in putamen and caudate also negatively correlated with FA (r= −0.800; p=0.014). The number of normal GFAP+

astrocytes in the putamen (**i**; r=0.700; p=0.043) and putamen and caudate (**j**; r=0.717; p=0.037) correlated with mean diffusivity. In putamen, the number of swollen GFAP astrocytes (**k**; r= −0.900; p=0.002) and the swollen-to-total GFAP+ astrocyte ratio (**l**; r= −0.933; p<0.001) correlated with FA. Symbols indicate piglets that received QA (open circle: 240 nmol, solid circle: 720 nmol, and solid triangle: 960 nmol), HI (solid squares), or sham procedure (open square).

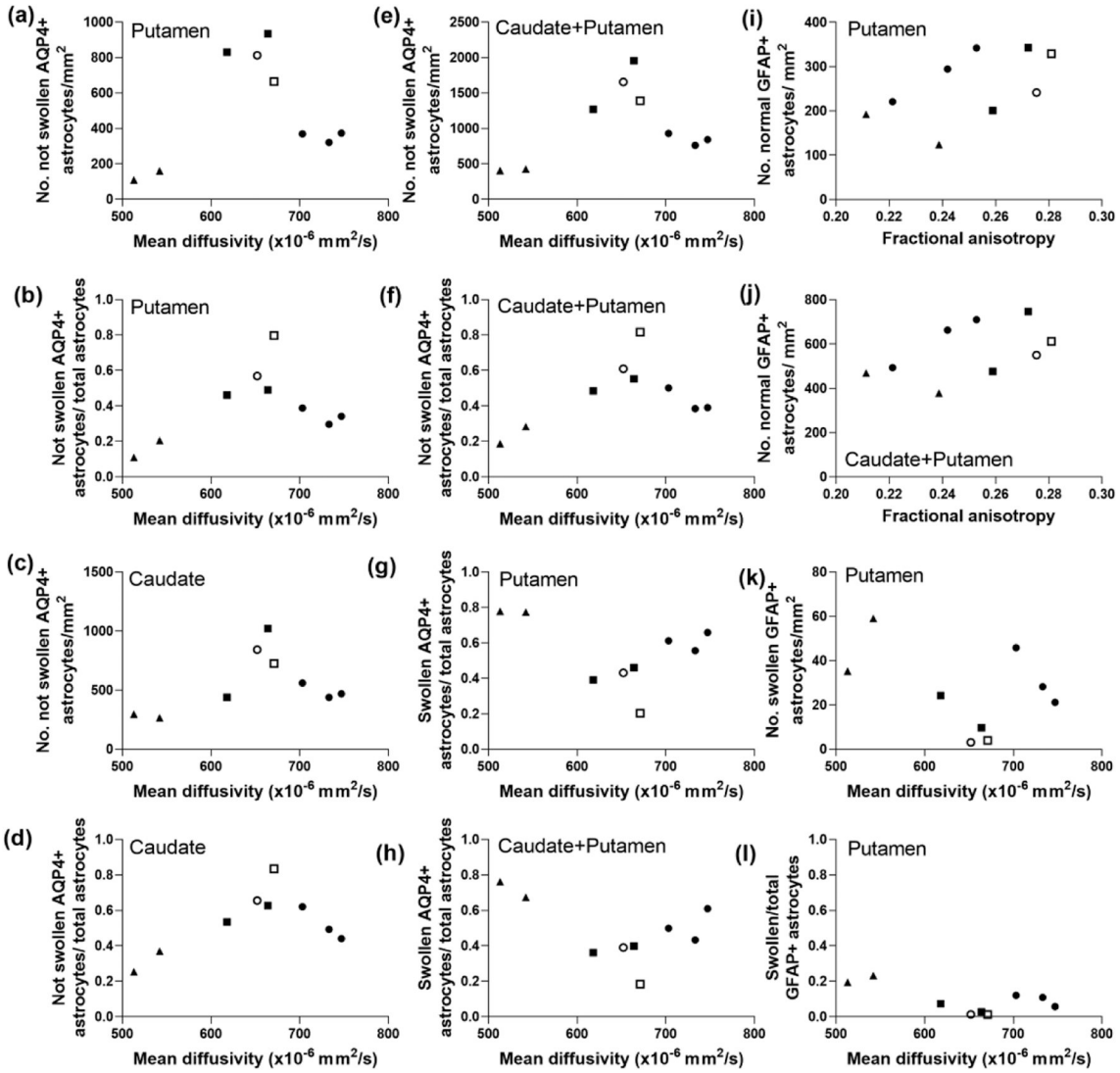

Figure 5.

Diffusion tensor imaging metrics that did not correlate with the morphology of aquaporin 4 (AQP4)- and glial fibrillary acidic protein (GFAP)-positive astrocytes in piglets with encephalopathy. **(a)** The number of AQP4+ astrocytes without swelling (r=0.167, p=0.678) and **(b)** the ratio of AQP4+ astrocytes without swelling to total astrocytes in putamen (r=0.233, p=0.552) were not related to mean diffusivity (MD). **(c)** Non-swollen AQP4+ astrocytes (r=0.393, p=0.295) and **(d)** their ratio to total astrocytes in caudate (r=0.283, p=0.463) did not correlate with MD. **(e)** The number of non-swollen astrocytes (r=0.200, p=0.613) and **(f)** their ratio (r=0.300, p=0.437) in putamen and caudate also did not correlate with MD. Additionally, MD showed no relationship to the swollen AQP4+ astrocyte-to-total astrocyte ratio in putamen (**g**; r= −0.183, p=0.644) or caudate and putamen combined (**h**; r= −0.557, p=0.123). The GFAP cell immunophenotyping showed that neither the number of normal GFAP+ astrocytes in putamen (**i**; r=0.600, p=0.097) nor the number in caudate and putamen (**j**; r=0.517, p=0.162) was related to fractional anisotropy. MD did not correlate with the number of swollen GFAP+ astrocytes (**k**; r= −0.233, p=0.552) or the ratio of

swollen to total GFAP+ astrocytes (**l**; r= −0.367, *p*=0.336) in putamen. Symbols indicate piglets that received QA (open circle: 240 nmol, solid circle: 720 nmol, and solid triangle: 960 nmol), HI (solid squares), or sham procedure (open square).

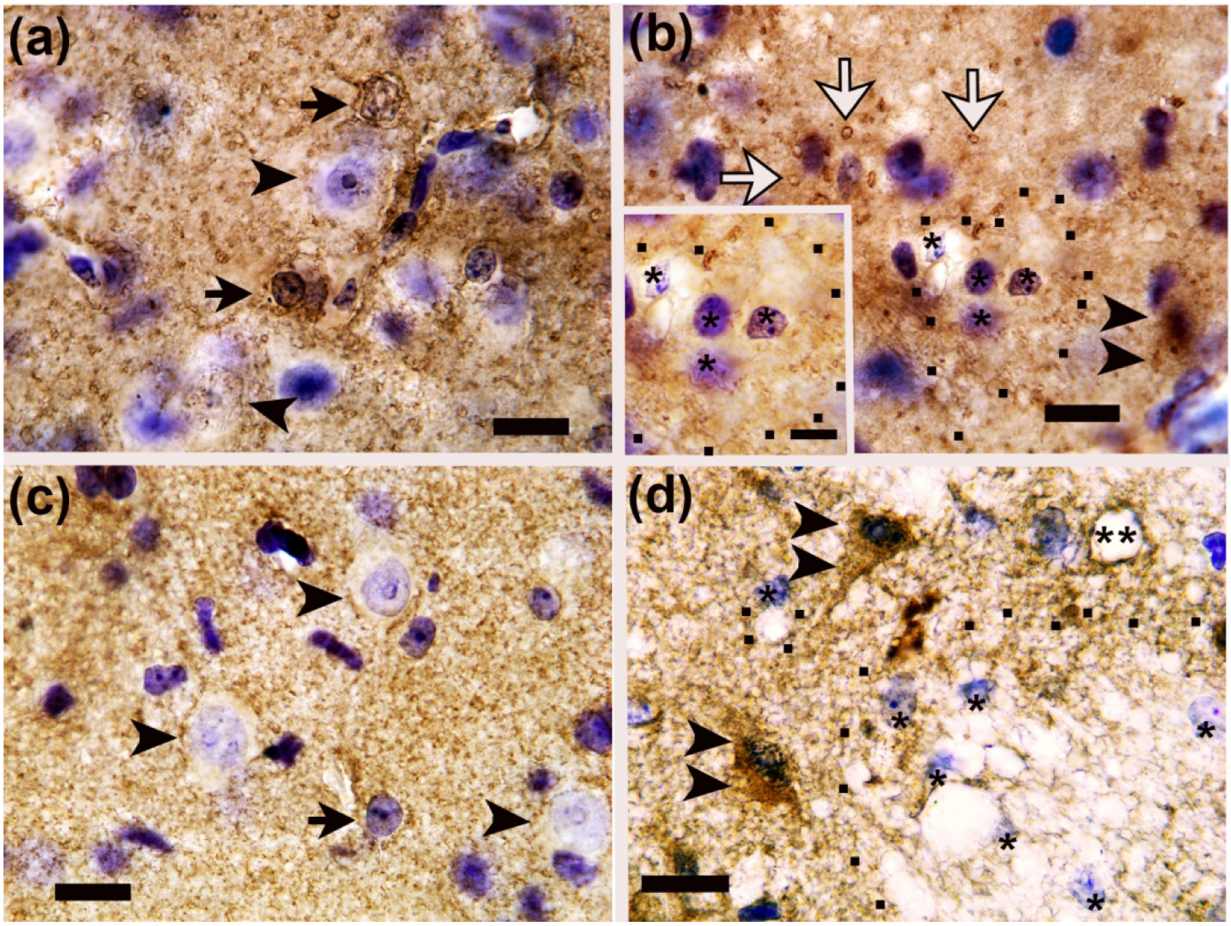

Figure 6.

Glutamate transporter 1 (GLT-1) immunohistochemistry identifies normal and pathological astrocytes in piglets with subacute striatal injury. **(a)** Putamen in a sham piglet shows normal GLT-1+ astrocytes (arrows). Normal neurons have GLT-1 processes decorating their cell membranes (arrowheads). **(b)** After hypoxia-ischemia (HI), astrocyte swelling is apparent in the putamen. The asterisks identify nuclei of swollen GLT-1+ astrocytes, and the black dots outline the swollen astrocyte bodies. The inset shows cytoplasm vacuoles of differing sizes in swollen astrocytes. White arrows denote swollen GLT-1+ astrocyte processes. The double arrowheads show a degenerating neuron with nuclear condensation and emerging GLT-1 cytoplasmic immunoreactivity. **(c)** After piglets were injected with 240 nmol quinolinic acid (QA), normal GLT-1+ astrocytes (arrow) and normal neurons with GLT-1+ processes along the cell membrane (arrowheads) were visible in putamen. **(d)** Injection of 960 nmol QA caused astrocyte swelling in putamen. Single asterisks identify the nuclei of swollen astrocytes, and black dots outline the swollen astrocyte cell bodies. The double arrowheads show degenerating neurons with necrotic chromatin condensation in the nucleus (Martin et al., 1998), GLT-1 enrichment in the cytoplasm, and a sharply angular cell body contour. The double asterisks identify a blood vessel with perivascular astrocyte labeling in apposition to the vessel exterior without apparent vasogenic edema. Photos were taken at 1000x with oil immersion. Main panel scale bars are 10 μm. Scale bar for panel B inset is 5 μm.

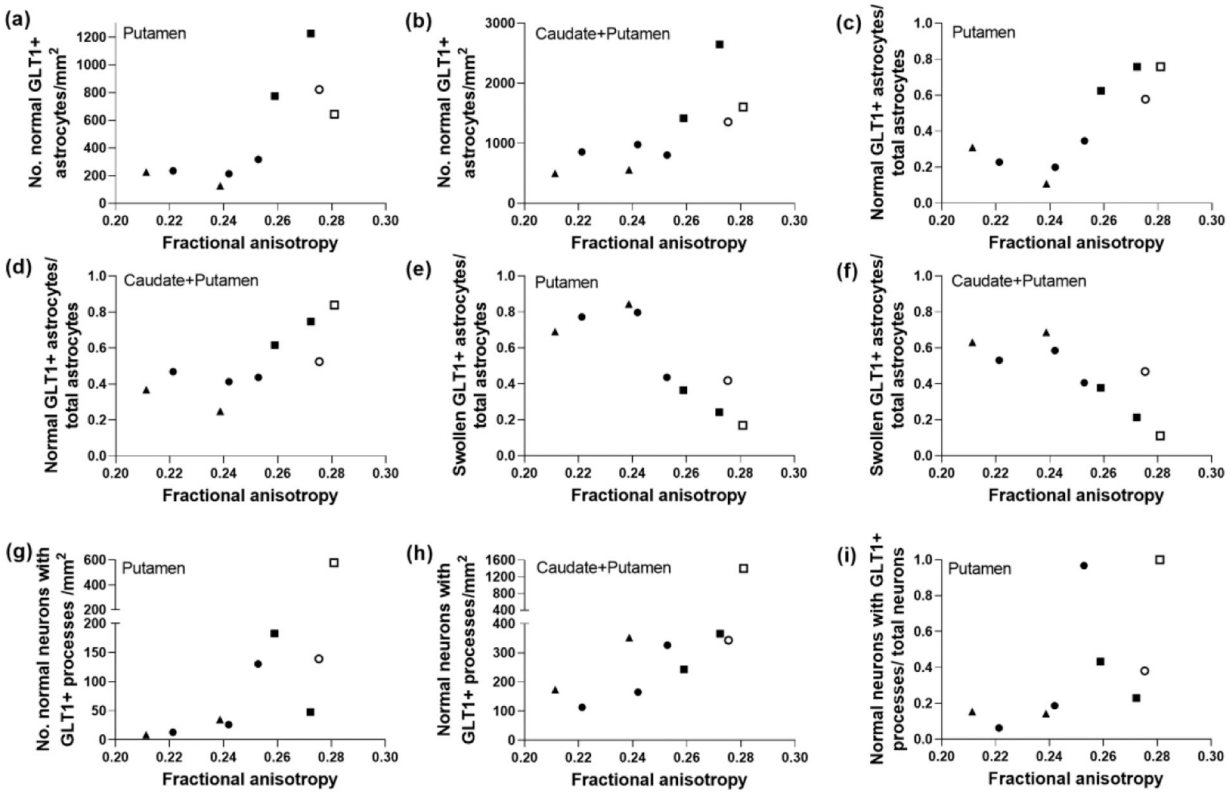

Figure 7.

Glutamate transporter 1 (GLT-1) labeling distinguished a relationship between astrocyte morphology and fractional anisotropy (FA) in piglets with excitotoxic and ischemic striatal damage. The number of normal GLT-1+ astrocytes in putamen (**a**; r=0.750; p=0.026) and caudate and putamen (**b**; r=0.833; p=0.008) correlated with FA, as did the ratio of normal GLT-1+ astrocytes to total astrocytes in putamen (**c**; r=0.800; p=0.014) and caudate and putamen (**d**; r=0.817; p=0.011). The ratio of swollen GLT-1+ astrocytes to total astrocytes also correlated with FA in putamen (**e**; r= −0.800; p=0.014) and caudate and putamen (**f**; r= −0.817; p=0.011). FA was also related to the number of normal neurons decorated by GLT-1+ processes on the neuronal cell membrane in putamen (**g**; r=0.900; p=0.002) and caudate and putamen (**h**; r=0.717; p=0.037). **(i)** The ratio of normal neurons with GLT-1+ processes to total neurons also correlated with FA in the putamen (r= 0.800; p=0.014). Symbols indicate piglets that received QA (open circle: 240 nmol, solid circle: 720 nmol, and solid triangle: 960 nmol), HI (solid squares), or sham procedure (open square).

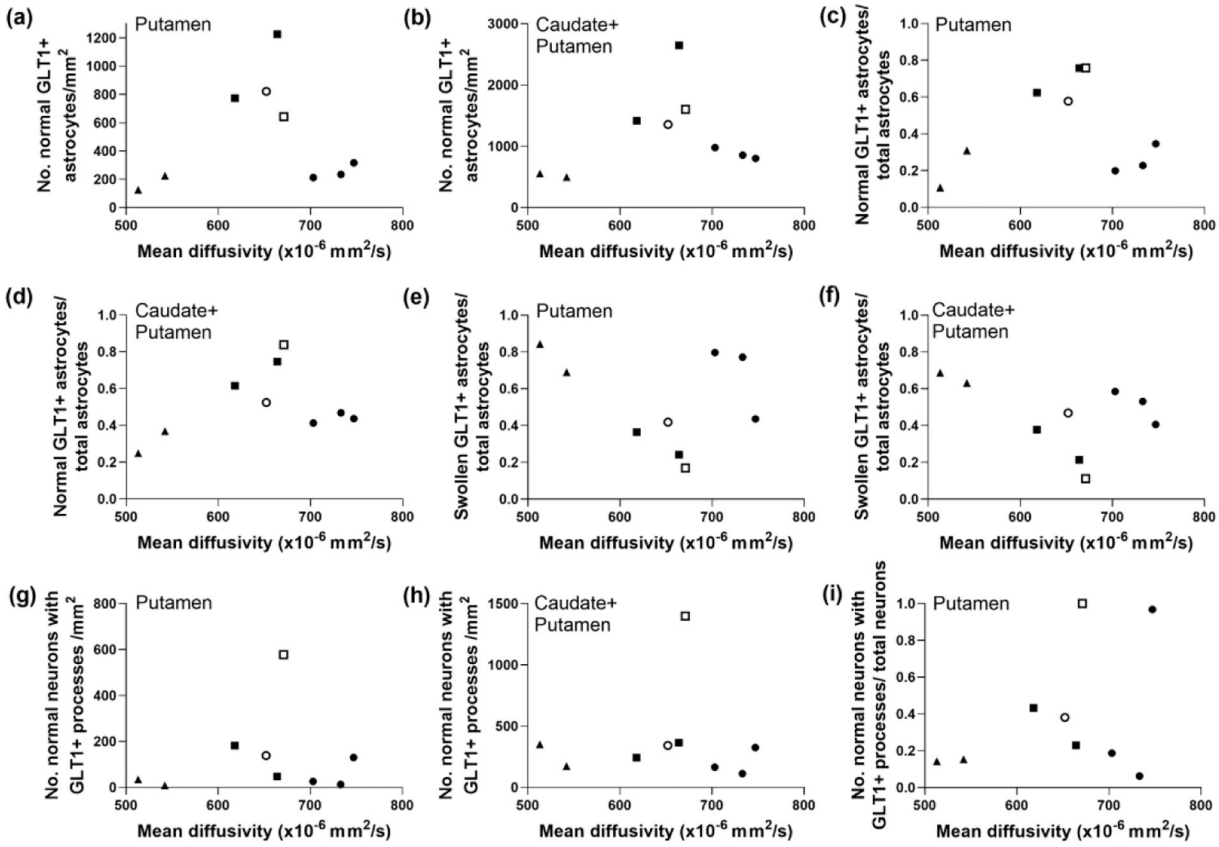

Figure 8.

Glutamate transporter 1 (GLT-1) immunoreactivity cell counts that were not correlated with mean diffusivity (MD) in piglets with subacute encephalopathy. The number of normal GLT-1+ astrocytes in neither putamen (**a**; r=0.117, *p*=0.776) nor caudate plus putamen (**b**; r=0.183, *p*=0.644) related to MD. Likewise the ratio of normal GLT-1+ astrocytes to total astrocytes in neither putamen (**c**; r=0.100, *p*=0.810) nor caudate and putamen (**d**; r=0.267, *p*=0.493) related to MD. The ratio of swollen GLT-1+ astrocytes to total astrocytes in putamen (**e**; r= −0.100, *p*=0.810) and caudate and putamen (**f**; r= −0.367, *p*=0.336) also showed no association with MD. The number of normal neurons with GLT-1+ astrocyte processes decorating the plasma cell membrane in putamen (**g**; r=0.050. *p*=0.912) and caudate and putamen (**h**; r= −0.250. *p*=0.521) was not correlated with MD. **(i)** Finally, the neuron ratio was also not associated with MD (r=0.250, *p*=0.521). Symbols indicate piglets that received QA (open circle: 240 nmol, solid circle: 720 nmol, and solid triangle: 960 nmol), HI (solid squares), or sham procedure (open square).

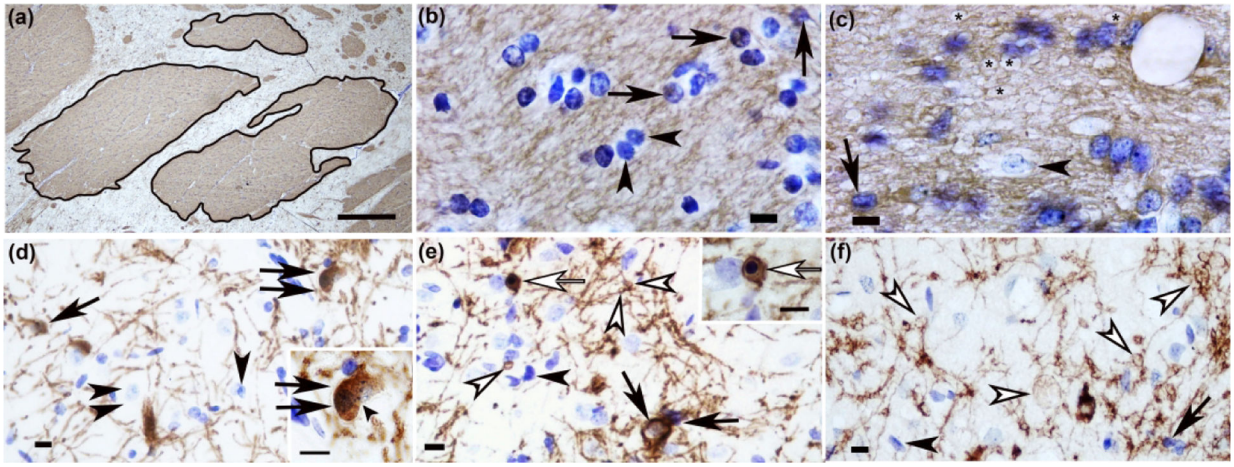

Figure 9.

CNPase immunohistochemistry identifies subacute damage to oligodendrocytes and their myelinating processes in piglet striatum with excitotoxic and ischemic injury. **(a)** In a coronal plane of the anterior striatum, the first three internal capsule bundles that were distinct from the corpus callosum and along the dorsal aspect of the lateral ventricle were outlined in ImageJ for area measurement. Cell counts and myelin swellings were divided by the sum area of the bundles. **(b)** Internal capsule of a sham piglet had normal CNPase+ oligodendrocytes with fine, delicate processes (arrows). The bundle matrix had a smooth and homogeneous meshwork of CNPase immunoreactivity. Arrowheads identify normal, CNPase-negative cells. **(c)** Injection of 720 nmol quinolinic acid (QA) caused myelin swellings in the internal capsule's matrix (asterisks). The myelin swellings created a spongiform pathology that attenuated the normal, homogeneous staining typical of white matter. The arrow identifies a normal, CNPase+ oligodendrocyte. The arrowhead shows a CNPase-negative cell. **(d)** Caudate of a sham pig showed a CNPase+ doublet cell with two nuclei, indicative of a recently divided oligodendrocyte (double black arrows). The inset shows the doublet cell's incompletely separated cytoplasm with two discernible nuclei. The inset's small arrowhead shows the separation between the two nuclei. The single arrow shows a normal, CNPase+ oligodendrocyte. The main panel's arrowhead identifies a CNPase-negative cell. The double arrowheads show a neuron. **(e)** After hypoxia-ischemia, oligodendrocyte process myelin swellings (white arrowheads) were apparent in putamen. An apoptotic, CNPase+ oligodendrocyte with nuclear condensation that formed a dark blue, round mass is identified by a white arrow in the main panel and inset. Normal CNPase+ oligodendrocytes (black arrows) and CNPase-negative cells (black arrowhead) are also shown. **(f)** Injection of 960 nmol QA led to development of oligodendrocyte process myelin swellings (white arrowheads). The arrow shows a CNPase+, normal oligodendrocyte. The black arrowhead shows a CNPase-negative cell. Panel A was photographed at 40x, and the scale bar is 0.25 mm. Panels B, C, and inset D were photographed at 1000x with oil immersion. The main panels D, E, and F were photographed at 400x. Scale bars in panels B-F are 10 μm.

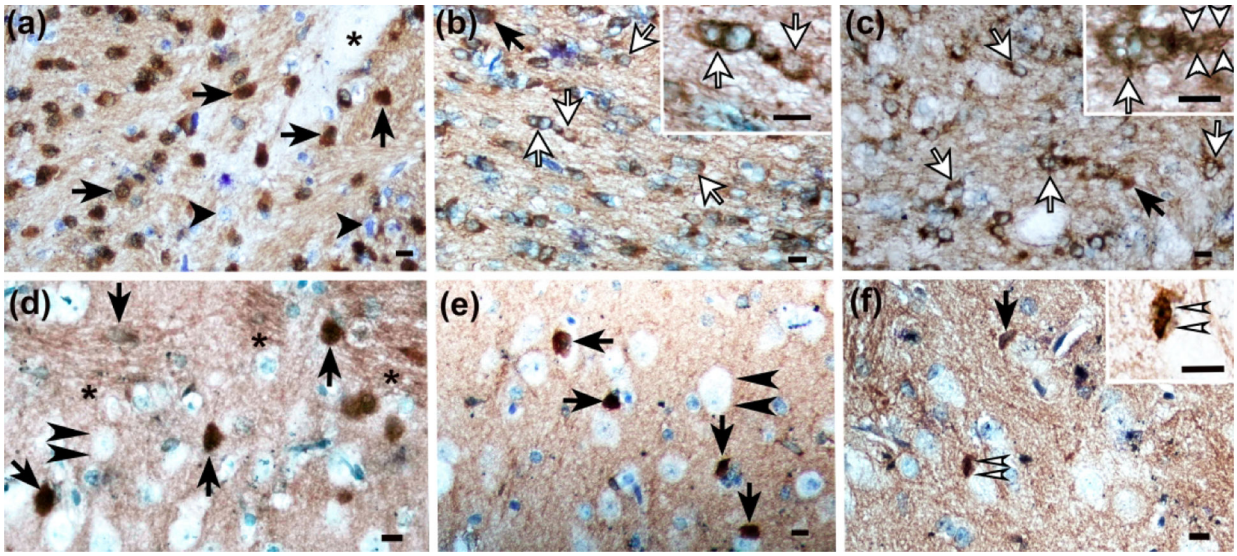

Figure 10.

Immunophenotyping and classification of normal and injured mature oligodendrocytes in piglet striatum with bridging integrator-1 (BIN1). **(a)** Internal capsule of a sham piglet showed normal oligodendrocytes with BIN1 immunoreactivity in the nucleus and cytoplasm (arrows). Normal BIN1-negative cells are identified by arrowheads. A neuron is marked by an asterisk. **(b)** The internal capsule of a piglet with hypoxia-ischemia had degenerating BIN1+ oligodendrocytes that exhibited vacuoles in the cell soma and nuclear exclusion of BIN1 (white arrows). The inset shows vacuoles and loss of BIN1 immunoreactivity. The black arrow indicates a normal BIN1+ oligodendrocyte that expresses BIN1 within the normal-appearing nucleus and cytoplasm. **(c)** In pigs that were injected with 960 nmol quinolinic acid (QA), multiple degenerating BIN1+ oligodendrocytes were identified as having vacuoles in the nucleus and cytoplasm alongside nuclear extrusion of BIN1 (white arrows). The arrowheads in the inset show vacuoles in the BIN1+ oligodendrocyte's processes. The black arrow identifies a normal BIN1+ oligodendrocyte. **(d)** Putamen in a sham piglet had normal BIN1+ oligodendrocytes (arrows). Neurons were not immunoreactive for BIN1 (double arrowheads). Each microscope field was randomly placed in putamen and included predominantly gray matter parenchyma plus some white matter bundles (asterisks). BIN1+ oligodendrocytes were counted in gray and white matter parenchyma within the putamen microscope field. **(e)** A sham piglet's caudate had normal BIN1+ oligodendrocytes (arrows) and BIN1-negative neurons (double arrowheads). **(f)** An apoptotic BIN1+ cell (double white arrows) and normal BIN1+ oligodendrocyte (arrow) in caudate of a piglet injected with 960 nmol QA. The apoptotic, karyorrhectic nuclear fragmentation is visible in the inset. Main panels were photographed at 400x. Insets B, C, and F were photographed at 1000x with oil immersion. All scale bars are 10 μm.

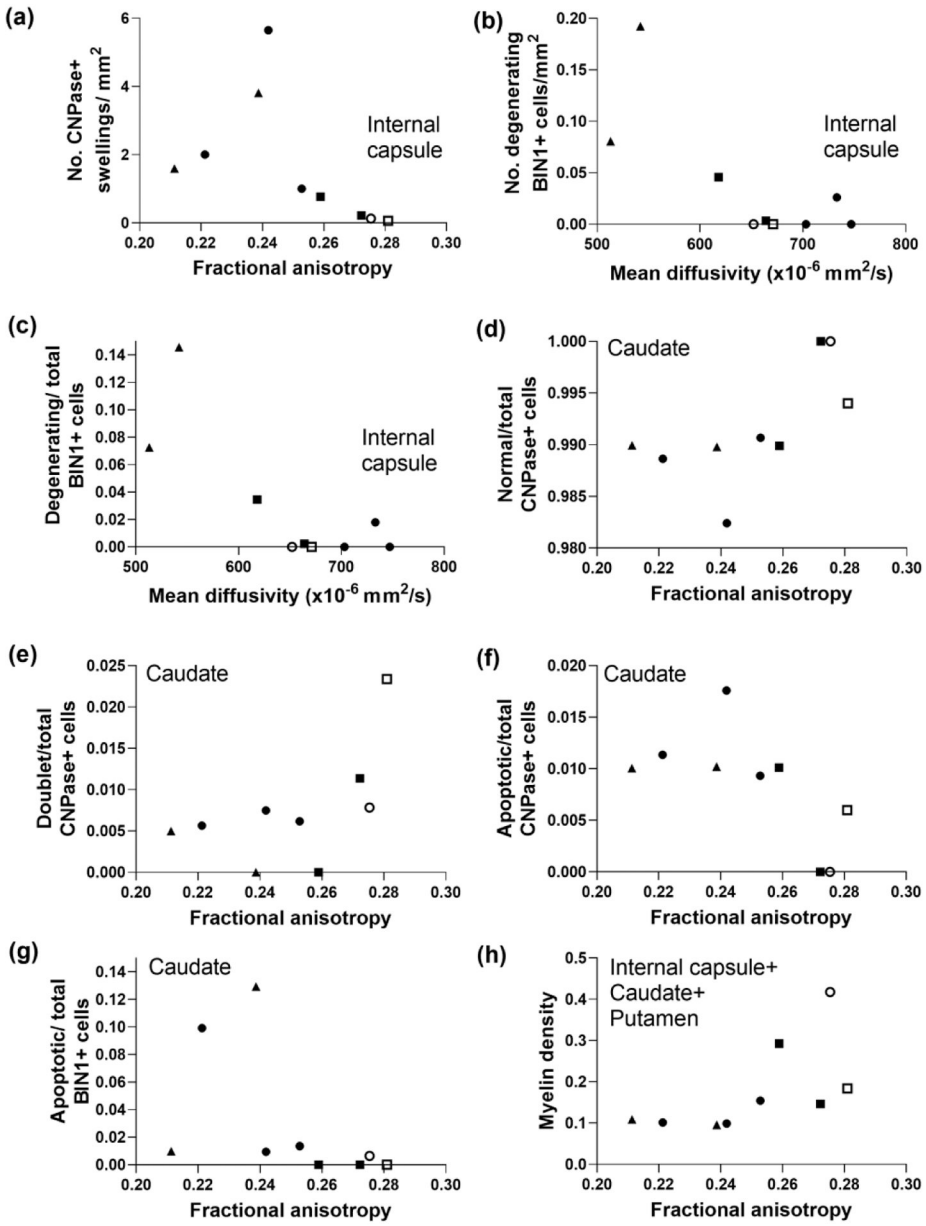

Figure 11.

Diffusion tensor imaging is associated with selective forms of oligodendrocyte degeneration and myelin injury in subacutely injured piglet striatum. **(a)** In the first three bundles of the internal capsule, the number of large CNPase+ myelin swellings correlated with fractional anisotropy (FA; r= −0.833, p=0.008). Mean diffusivity (MD) was associated with the number of degenerating BIN1+ cells (**b**; r= −0.696, p=0.046) and the ratio of degenerating BIN1+ cells to total BIN1+ cells in the internal capsule (**c**; r= −0.696, p=0.046). FA correlated with the ratios of normal-to-total CNPase+ cells (**d**; r=0.695, p=0.045), doublet-to-total CNPase+ cells (**e**; r=0.695, p=0.045), apoptotic-to-total CNPase+ cells (**f**; r= −0.695, p=0.045), and apoptotic-to-total BIN1+ cells (**g**; r= −0.763, p=0.024) in caudate. **(h)** Myelin density measured by Luxol fast blue stain in caudate, internal capsule, and putamen

correlated with FA (r=0.733, p=0.031). Symbols indicate piglets that received QA (open circle: 240 nmol, solid circle: 720 nmol, and solid triangle: 960 nmol), HI (solid squares), or sham procedure (open square).

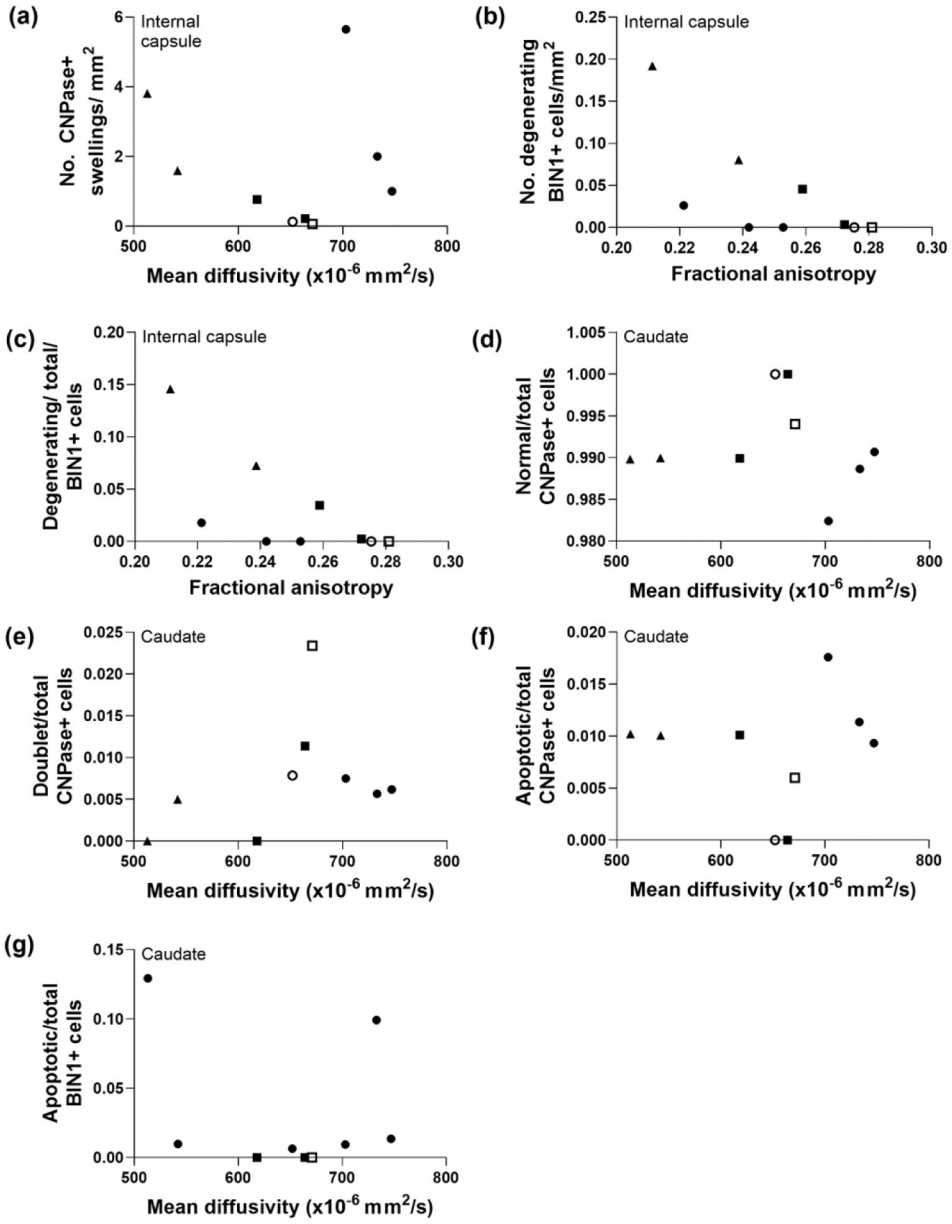

Figure 12.

Myelin and oligodendrocyte markers that did not correlate with diffusion tensor imaging in striatum of piglets with subacute injury. **(a)** The number of large CNPase+ myelin swellings in the internal capsule did not correlate with mean diffusivity (MD; r=0.000, p>0.999). **(b)** The number of degenerating BIN1+ cells (r= −0.662, p=0.061) and **(c)** the ratio of degenerating BIN1+ cells to total BIN1+ cells (r= −0.662, p=0.061) in internal capsule were not associated with fractional anisotropy (FA). In caudate, the ratios of **(d)** normal-to-total CNPase cells (r= −0.433, p=0.250), **(e)** doublet-to-total CNPase cells (r=0.469, p=0.204), **(f)** apoptotic-to-total CNPase+ cells (r=0.075, p=0.853), and **(g)** apoptotic-to-total BIN1+ cells (r=0.034, p=0.946) did not correlate with MD. Symbols indicate piglets that received QA

(open circle: 240 nmol, solid circle: 720 nmol, and solid triangle: 960 nmol), HI (solid squares), or sham procedure (open square).

Table 1.

Primary antibodies

Antibody	Company	Species	Clone	Concentration	Identify
AQP4	LS Bio (Seattle, WA)	Rabbit	LS-C413484	1:25	Astrocytes involved in regulating brain water
BIN1	Proteintech (Rosemont, IL)	Rabbit	Polyclonal	1:200	Mature, myelinating oligodendrocytes
CNPase	Millipore Sigma (Burlington, MA)	Mouse	11–5B	1:50	Oligodendrocytes and myelinating processes
GFAP	Agilent Dako, (Santa Clara, CA)	Rabbit	Polyclonal	1:200	Parenchymal and perivascular astrocytes
GLT-1	Developed and validated by author LJM	Rabbit	Polyclonal	1:100	Astrocytes involved in excitatory neurotransmission and glutamate reuptake

2′,3′-cyclic nucleotide 3′-phosphodiesterase, CNPase. Aquaporin 4, AQP4. Bridging integrator-1, BIN1. Glial fibrillary acidic protein, GFAP. Glutamate transporter 1, GLT-1.